Targeting bromodomain plant homeodomain finger transcription factor reverses melanoma immune evasion via the p53/PD-L1 axis: A study integrating machine learning identification and methapyrilene repurposing

XIA KANG[1*], JIANG HE[2*], XIAOYING YAO[3], XIAOWAN ZHANG[4], BIYU SHEN[1] and JING YANG[5-7]

[1]Department of Oncology, West China Hospital Sichuan University Jintang Hospital/Jintang First People's Hospital, Chengdu, Sichuan 610400, P.R. China; [2]Department of Internal Medicine, Central Medical Center of Sichuan Provincial Prison Administration, Chengdu, Sichuan 610400, P.R. China; [3]Department of Ultrasound, The General Hospital of Western Theater Command, Chengdu, Sichuan 610400, P.R. China; [4]Department of The First Cadre, The General Hospital of Western Theater Command, Chengdu, Sichuan 610400, P.R. China; [5]Experimental Teaching Center of Biotechnology, School of Bioscience and Technology, Chengdu Medical College, Chengdu, Sichuan 610500, P.R. China; [6]Key Laboratory of Target Discovery and Protein Drug Development in Major Diseases at Chengdu Medical College of Sichuan Province, Chengdu, Sichuan 610500, P.R. China; [7]Irradiation Preservation and Effect Key Laboratory of Sichuan Province, Chengdu, Sichuan 610500, P.R. China

Received June 1, 2026; Accepted October 26, 2026

DOI: 10.3892/mmr.2026.14087

Abstract. Primary non-response and acquired resistance limit immunotherapy efficacy in melanoma. Tumor-cell transcriptional programs influence immune-checkpoint signaling and susceptibility to T cell-mediated killing. The present study aimed to identify actionable tumor-intrinsic regulators of immune escape and evaluate their therapeutic tractability. Transcriptomic data from four melanoma immunotherapy datasets were integrated for differential expression analysis. Candidate genes were selected using three machine learning (ML) approaches. Subsequently, eight ML models and the SHapley Additive exPlanations analysis were used to prioritize response-associated features. Pathway enrichment analysis explored biological pathways associated with the top-ranked candidate gene. Drug-gene interaction analysis, molecular docking and molecular dynamics simulations identified therapeutic candidates. Gene overexpression and knockdown models were established by plasmid and short hairpin RNA transfection, respectively. Colony-formation, Transwell, western blotting, cellular thermal shift, drug affinity-responsive target stability and T-cell co-culture assays were performed. Six feature genes were identified. Particularly, bromodomain plant homeodomain finger transcription factor (BPTF) ranked highest and was negatively associated with immune therapy response. BPTF-high samples demonstrated negative enrichment of the p53 pathway. *In vitro*, BPTF overexpression notably promoted melanoma clonogenic growth and invasion, suppressed p53 signaling, increased mouse double minute 2 (MDM2) and programmed death-ligand 1 (PD-L1) expression, and impaired $CD8^+$ T-cell activation and cytotoxicity. BPTF knockdown produced reciprocal effects. Chromatin immunoprecipitation-quantitative PCR and dual-luciferase assays supported BPTF-mediated repression of *TP53* and activation of *CD274*. Methapyrilene demonstrated stable predicted binding to BPTF, increased BPTF thermal and proteolytic stability, and attenuated BPTF-associated malignant and immune-evasive phenotypes. The combination with PD-L1 blockade enhanced tumor-cell killing and T-cell effector responses compared with

Correspondence to: Dr Biyu Shen, Department of Oncology, West China Hospital Sichuan University Jintang Hospital/Jintang First People's Hospital, 886 Jinguang Road, Zhao, Jintang, Chengdu, Sichuan 610400, P.R. China
E-mail: 13568902872@163.com

Dr Jing Yang, Experimental Teaching Center of Biotechnology, School of Bioscience and Technology, Chengdu Medical College, 783 Xindu Avenue, Xindu, Chengdu, Sichuan 610500, P.R. China
E-mail: jingyang@cmc.edu.cn

*Contributed equally

Abbreviations: BPTF, bromodomain plant homeodomain finger transcription factor; ML, machine learning; SHAP, SHapley Additive exPlanations; PCA, principal component analysis; LASSO, least absolute shrinkage and selection operator; SVM-RFE, support vector machine-recursive feature elimination; RF, random forest; GBM, gradient boosting machine; CV, cross-validation; ssGSEA, single-sample gene set enrichment analysis; AUC, area under the curve; ChIP, chromatin immunoprecipitation; CETSA, cellular thermal shift assay; DARTS, drug affinity-responsive target stability; MFI, mean fluorescence intensity; MDM2, mouse double minute 2; OOB, out-of-bag; PD-1, programmed cell death protein-1; PD-L1, programmed death-ligand 1; LDH, lactate dehydrogenase; NURF, nucleosome remodeling factor; YY1, Yin-Yang 1

Key words: melanoma, immune escape, ML, BPTF, methapyrilene

either treatment alone. In conclusion, BPTF associates melanoma progression with immune escape through the p53/PD-L1 axis. Methapyrilene interacts with BPTF and provides a lead scaffold for developing BPTF-directed agents in combination with PD-L1 blockade to overcome immunotherapy resistance in the future.

Introduction

Melanoma is the most lethal form of skin cancer, with >300,000 new cases and ~61,550 associated deaths worldwide in 2021, representing a growing global public health challenge (1). This mortality burden reflects its propensity for metastatic dissemination and therapeutic resistance (2). Clinical data demonstrated that the 5-year survival rate following surgical resection of early-stage localized melanoma classified according to the American Joint Committee on Cancer staging system is 95-100% for stage I and 65-92.8% for stage II disease. However, ~30% of primary tumors progress to metastatic disease for which the 5-year survival rate declines to 5-15% (3). Immune checkpoint blockade (ICB) and targeted therapies have markedly improved outcomes in advanced melanoma but acquired resistance and primary non-response still result in disease progression (4,5). Defining actionable mechanisms of resistance is therefore key to improving treatment responses and prolonging disease control in the future.

Melanoma exhibits extensive genomic, epigenetic and phenotypic plasticity shaped by ultraviolet-induced DNA damage, recurrent oncogenic alterations and lineage-specific cellular programs (6,7). Despite its high mutational burden and capacity for neoantigen generation, melanoma frequently evades immune control (8). This discordance indicates that tumor antigenicity alone does not determine the response to immunotherapy. Tumor cells can actively evade immune surveillance through altered antigen presentation, sustained immunosuppressive signaling, enhanced inhibitory checkpoint signaling and impaired $CD8^+$ T-cell activation and cytotoxicity (9,10). Among these mechanisms, upregulation of programmed death-ligand 1 (PD-L1) represents a major tumor-intrinsic mechanism that restrains antitumor T-cell responses (9,11). These immune-evasive adaptations may intersect with mechanisms that support tumor-cell survival, invasion and phenotypic plasticity (10). However, the upstream regulators associating malignant progression with immunosuppression remain incompletely characterized.

Increasing evidence implicates tumor-cell transcriptional and epigenetic states in melanoma resistance to immunotherapy. Single-cell analyses of human melanoma have identified pretreatment malignant cell programs associated with T-cell exclusion and resistance to ICB (12). Functional studies have further demonstrated that chromatin regulators reshape transcriptional programs and modulate chromatin accessibility. These changes can alter interferon (IFN) responsiveness, antigen presentation, tumor immunogenicity and susceptibility to cytotoxic T-cell killing (13-15). Chromatin-associated regulators may therefore coordinate numerous components of immune resistance, including checkpoint-ligand expression. However, which regulators are reproducibly associated with clinical non-response, functionally contribute to melanoma immune evasion and are amenable to pharmacological intervention remain to be elucidated.

Patient-derived transcriptomic profiles from immunotherapy cohorts provide a clinically relevant basis for identifying chromatin-associated regulators of immune resistance; however, inter-cohort heterogeneity and limited sample sizes can compromise the reproducibility of candidate regulators identified from individual datasets. Machine learning (ML) can integrate complex expression patterns and prioritize response-associated molecular features (16,17). Interpretable methods, such as SHapley Additive exPlanations (SHAP), further clarify the contribution of each molecular feature to model predictions (18). Therefore, the present study integrated cross-cohort transcriptomic analysis with bidirectional genetic perturbation, mechanistic assays, tumor cell-T cell co-culture models and pharmacological target-engagement evaluation. The present study aimed to identify and validate a druggable tumor-intrinsic regulator of melanoma immune escape, thereby establishing a mechanistic rationale for strategies to overcome immunotherapy resistance in the future.

Materials and methods

Data collection and preprocessing

Dataset acquisition. In the present study, four melanoma immunotherapy datasets were obtained from public databases: Melanoma-GSE91061 (19), -phs000452 (20), -PRJEB23709 (21) and -GSE122220 (22). GSE91061 and GSE122220 are deposited in the Gene Expression Omnibus (https://www.ncbi.nlm.nih.gov/geo/), phs000452 in the database of Genotypes and Phenotypes (https://www.ncbi.nlm.nih.gov/gap/) and PRJEB23709 in the European Nucleotide Archive (https://www.ebi.ac.uk/ena/). Detailed information regarding the data sources, original publications, treatment regimens, sequencing platforms, sampling times and clinical responses distribution is provided in Tables SI-IV. Gene expression data (.exp.csv format) and corresponding clinical information (.clinical.csv format) were downloaded for each dataset. Clinical response categories were classified according to the Response Evaluation Criteria in Solid Tumors (RECIST) or RECIST version 1.1 annotations provided in the original studies (23). Samples were classified into 'responder' or 'non-responder' groups based on the immunotherapy response status recorded in the clinical data. For cohorts containing numerous samples from the same patient, only a single pretreatment sample per patient was retained for the primary analysis. This restriction preserved patient-level independence and prevented data leakage between the model training and validation folds.

Data normalization and quality control. Expression data were processed separately based on the platform and data format. RNA-sequencing datasets were transformed and normalized as appropriate for the expression units provided by the original data sources. A $\log_2$ transformation was applied when quantile analysis indicated raw data characteristics (75th percentile >100 or a range >50 with a positive 25th percentile). The GSE122220 microarray dataset was quantile-normalized using the 'normalizeBetweenArrays()' function from the 'limma' package (version 3.56.2; https://bioconductor.org/packages/limma/) in R software (version 4.3.0; R Foundation for

Statistical Computing; https://www.r-project.org/). Duplicate gene probes were averaged using the 'avereps()' function.

Batch effect correction and data integration. Genes shared across the four datasets were identified before data integration. Among these genes, high-variance genes were selected (the top 3,000 genes or 20% of the intersecting genes, whichever was smaller) to improve the effectiveness of batch correction. The 'ComBat' method implemented in the 'sva' package (version 3.48.2) was used to remove batch effects, with the first dataset as the reference batch. Immunotherapy response status was included in the 'ComBat' model matrix to preserve response-associated biological variation. Principal component analysis (PCA) was performed before and after batch correction. Data distributions were visualized using the 'ggplot2' package (version 3.4.2; https://ggplot2.tidyverse.org/).

Differential gene expression analysis. Differential gene expression analysis was conducted using the 'limma' package (version 3.56.2). A design matrix encoded immunotherapy response status and the contrasts were made comparing non-responder with responder samples. Positive $\log_2$fold-change ($\log_2$FC) values indicated higher expression in non-responders, whereas negative values indicated lower expression compared with responders. $P<0.05$ and $\log_2FC>0.25$ were considered to indicate a statistically significant difference.

Feature selection

Directionally constrained candidate-gene selection. Only genes upregulated in the non-responder group were retained for feature selection. Melanoma resistance to ICB can be sustained by transcriptionally activated immunosuppressive programs, including checkpoint-ligand induction, immunosuppressive metabolism and tumor-cell programs that promote T-cell exclusion (24-26). As these gain-of-function alterations are more directly amenable to inhibitory intervention, upregulated genes were prioritized as potentially actionable mediators of immune tolerance and treatment resistance.

Least absolute shrinkage and selection operator (LASSO) regression. LASSO regression analysis was performed using the 'glmnet' package (version 4.1-7; https://glmnet.stanford.edu/) with 10-fold cross-validation (CV). The optimal λ value ('lambda.min' function) was determined through CV and genes with non-zero coefficients were retained as candidate features.

Support vector machine-recursive feature elimination (SVM-RFE). SVM-RFE recursively eliminated features based on their importance in the SVM-based classification (27). CV was performed with 10 folds and feature importance was ranked based on the mean rank across validation sets.

Random forest (RF). RF analysis was conducted using the 'randomForest' package (version 4.7-1.1). Forests were grown with up to 500 decision trees. Feature importance was calculated using the mean decrease in the Gini coefficient. Genes with importance scores >1 were considered to indicate significant features. The optimal number of trees was determined by identifying the number associated with the minimum out-of-bag (OOB) error rate.

Feature integration. Venn diagram analysis was performed using 'ggvenn' package (version 0.1.10; https://yanlinlin82.github.io/ggvenn/) to identify genes shared among the three ML methods. The intersection of the genes identified by all three methods was retained to constitute the final feature gene set. The chromosomal locations of the resulting genes were annotated against Ensembl/GRCh38 annotations (28) using the 'biomaRt' package (version 2.56.1; https://bioconductor.org/packages/biomaRt/).

Model construction, evaluation and interpretation

Model training and evaluation. In total, eight ML models were constructed using the six shared feature genes: RF ('rf' package), SVM ('svmRadial' package; https://cran.r-project.org/package=kernlab), extreme gradient boosting ('XGBoost' and 'xgbTree' packages; https://cran.r-project.org/package=xgboost), gradient boosting machine ('GBM' package), naive Bayes ('naive_bayes' package; https://cran.r-project.org/package=naivebayes), k-nearest neighbors ('knn' package; https://topepo.github.io/caret/), logistic regression ('glmnet' package) and neural network ('nnet' package; https://cran.r-project.org/package=nnet). Model training and hyperparameter tuning were performed using the 'caret' package (version 6.0-94). A 5-fold CV repeated three times was used for model evaluation. Receiver operating characteristic curves were generated and the corresponding areas under the curve (AUCs) were calculated to assess model performance.

SHAP-based model interpretation. SHAP values for the best-performing model were calculated using the 'kernelshap' package (version 0.3.7; https://modeloriented.github.io/kernelshap/) with 50 permutations. Global feature importance was determined by the mean absolute SHAP values. SHAP dependence plots were used to examine the relationship between individual gene expression and model output. Positive SHAP values indicated that a feature increased the predicted probability of response to immunotherapy. Feature importance was additionally evaluated across all eight algorithms using model-appropriate measures, including SHAP values, Gini importance, absolute standardized coefficients and permutation importance. As these measures were expressed on different scales, cross-model consistency was assessed using within-model feature rankings rather than their raw importance values.

Pathway enrichment analysis. Single-sample gene set enrichment analysis (ssGSEA) was performed using the 'Gene Set Variation Analysis' package (version 1.48.3). Kyoto Encyclopedia of Genes and Genomes (KEGG) pathway gene sets ('c2.cp.kegg.Hs.symbols.gmt' file) and Hallmark gene sets ('Hallmark gene sets.gmt' file) were obtained from the Molecular Signatures Database (version 2023.1.Hs; https://www.gsea-msigdb.org/gsea/msigdb/). Descriptions of these gene set collections are available at https://www.gsea-msigdb.org/gsea/msigdb/human/collections.jsp. Samples were divided into bromodomain plant homeodomain finger transcription factor (BPTF)-high and -low groups based on the median BPTF expression. ssGSEA scores were calculated for each pathway in each sample. Pathway scores were compared between the two groups using the 'limma' package. The Benjamini-Hochberg method was applied to correct for multiple testing (29). Pathways with $P<0.05$ were considered to indicate differentially enriched pathways. Positive test

statistics indicated higher pathway scores in the BPTF-high group.

Drug-gene interaction analysis. Drug-gene interaction data were obtained from the Drug Signatures Database (DSigDB; version 1.0). The data were processed to extract drug names, target genes and regulatory directions (upregulation or downregulation). Enrichment analysis was performed using the 'clusterProfiler' package (version 4.8.3; https://bioconductor.org/packages/clusterProfiler/) with a custom 'TERM2GENE' mapping. The direction of each drug-gene association was determined from the gene expression changes reported in the DSigDB. Compounds were classified into three categories: i) Inhibitory drugs, which predominantly downregulated target genes and were considered potential therapeutic candidates; ii) promoting drugs, which predominantly upregulated target genes and should therefore be avoided; and iii) modulatory drugs, which exerted mixed effects and required further validation. Drug-gene interactions were validated using the Drug-Gene Interaction Database (version 5.0; https://www.dgidb.org/). Drug-gene interaction networks were constructed using 'igraph' package (version 1.5.0; https://r.igraph.org/). Node colors represented drug classifications: Blue for inhibitory drugs, red for promoting drugs and purple for modulatory drugs.

Molecular docking analysis. Molecular docking was performed using the Computer-Aided Drug Design platform (https://cadd.labshare.cn/cb-dock/). Small molecule structures were obtained from the PubChem database (https://pubchem.ncbi.nlm.nih.gov/) and protein structures were retrieved from the Research Collaboratory for Structural Bioinformatics Protein Data Bank (https://www.rcsb.org/). Protein preparation included the removal of crystallographic solvent molecules and irrelevant ligands, the addition of hydrogen atoms and the assignment of appropriate charges. Candidate binding pockets were identified using the pocket-detection module implemented in the platform. Methapyrilene was subsequently docked into each predicted pocket using AutoDock Vina software (version 1.1.2; https://vina.scripps.edu/). Binding poses were ranked according to their Vina scores, and the top-ranked pose was selected for subsequent molecular dynamics simulation. AU1 was included as a reference BPTF ligand.

Molecular dynamics simulation. The docking results were further evaluated by molecular dynamics simulations using AMBER 22 (30) and AmberTools 23 (31). These simulations assessed the stability of the predicted BPTF-methapyrilene complex under dynamic conditions. A total of three systems were constructed under identical simulation conditions: Ligand-free BPTF (Apo BPTF), the BPTF-methapyrilene complex and the BPTF-AU1 reference complex. Each system was subjected to energy minimization, equilibration and a 100-nsec production simulation. Global conformational stability was assessed using the backbone root-mean-square deviation. Residue-level flexibility was evaluated using the root-mean-square fluctuation, with particular attention to the ZA and BC loop regions, which connect the αZ-αA and αB-αC helices, respectively, and flank the acetyl-lysine-binding pocket of the BPTF bromodomain. Ligand-protein binding free energy (ΔG_bind) was estimated using the molecular mechanics/generalized Born surface area (MM/GBSA) method (32).

In vitro assays

Cell lines and culture conditions. Human melanoma SK-MEL-28 (cat. no. CL-0717; Procell Life Science & Technology Co., Ltd.), A375 (cat. no. B26319; Sichuan Bio Biotech Co., Ltd.), SK-MEL-2 (cat no. CL-0706; Procell Life Science & Technology Co., Ltd.) and MeWo (cat. no. CL-0877; Procell Life Science & Technology Co., Ltd.) cell lines were cultured in high-glucose DMEM (cat. no. PMK-M002; Hubei Bioprimacy Co., Ltd.) culture medium supplemented with 10% FBS (cat. no. 10099141C; Gibco; Thermo Fisher Scientific, Inc.) and 1% penicillin/streptomycin (cat. no. PMK0702; Hubei Bioprimacy Co., Ltd.) at 37˚C in an incubator containing 5% CO_2.

BPTF overexpression and knockdown. BPTF gain- and loss-of-function models were established by transfecting cells with a BPTF overexpression plasmid or BPTF-targeting short hairpin RNA (shRNA/sh), respectively. Full-length human BPTF complementary DNA (National Center for Biotechnology Information Reference Sequence: NM_004459.7; https://www.ncbi.nlm.nih.gov/nuccore/NM_004459.7/) was cloned into the pCMV6-Entry vector (cat. no. V011173; NovoPro Bioscience Inc.) for BPTF overexpression. The empty pCMV6-Entry vector lacking the BPTF insert was used as the negative/vector control. For BPTF knockdown, shBPTF-1 [sense (S): 5'-CGC CTTATGATGAATCTAAAT-3'; antisense (AS): 5'-ATT TAGATTCATCATAAGGCG-3'] and shBPTF-2 (S: 5'-GCG GCAGCTAATGAAGAAATT-3'; AS: 5'-AATTTCTTC ATTAGCTGCCGC-3') were cloned into the pLKO.1 vector (cat. no. 8453; Addgene, Inc.) and non-targeting shRNA control (shNC; S: 5'-CAACAAGATGAAGAGCACCAA-3'; AS: 5'-TTGGTGCTCTTCATCTTGTTG-3') was used as the negative control. Plasmids including BPTF shRNA constructs and shNC were custom-constructed by General Biosystems (Anhui) Co., Ltd.

Cells in 6-well plates were transfected with 2.5 μg plasmid DNA per well were transfected using Lipofectamine® 3000 (cat. no. L3000001; Thermo Fisher Scientific, Inc.) according to the manufacturer's instructions. For each well, 3.75 μl Lipofectamine 3000 and 5 μl P3000 reagent were used to prepare DNA-lipid complexes in Opti-MEM (cat. no. 31985070; Thermo Fisher Scientific, Inc.). The complexes were incubated at room temperature for 5 min before 250 μl was added to each well. Cells were maintained at 37˚C in a humidified atmosphere containing 5% CO_2. For experiments evaluating BPTF function alone, the overexpression model comprised the vector and BPTF-overexpressed (BPTF-OE) groups, whereas the knockdown model comprised the shNC and shBPTF groups. Cells used for these experiments were collected 48 h after transfection. Both shBPTF constructs were used in the initial loss-of-function experiments, whereas shBPTF-1 was used in the subsequent mechanistic and pharmacological experiments. SK-MEL-28 and A375 cells were used for both gain- and loss-of-function analyses. SK-MEL-2 and MeWo cells were used only to initially validate BPTF overexpression.

Drug treatment. Methapyrilene (cat. no. HY-111130; MedChemExpress) was dissolved in DMSO and administered at a final concentration of 10 μM for 48 h. An equivalent volume of DMSO was added to the vehicle-control groups, and the final DMSO concentration was 0.1% (v/v) in all groups. Drug treatment was initiated 24 h after plasmid or shRNA transfection.

Functional assays. i) Colony formation assay. SK-MEL-28 and A375 cells were seeded in 6-well plates at 500 cells/well in 2 ml complete medium, with three replicate wells per condition, and maintained at 37˚C with 5% CO_2. After attachment for 24 h, cells were transfected with the indicated constructs as aforementioned. For drug-treatment experiments, 10 μM methapyrilene or vehicle was added 24 h after transfection for 48 h; the final DMSO concentration was adjusted to 0.1% (v/v) in all groups. The medium was then replaced with drug-free complete medium, and cells were cultured until day 14 after seeding. Colonies were washed with PBS, fixed with 4% paraformaldehyde (cat. no. BL539A; Beijing Labgic Technology Co., Ltd.) for 15 min and stained with 0.1% (w/v) crystal violet (cat. no. BL802A; Beijing Labgic Technology Co., Ltd.) for 20 min, both at room temperature. After rinsing with water and air-drying, colonies containing >50 cells were counted using ImageJ software (version 1.54g; National Institutes of Health).

ii) Transwell migration/invasion assays. Migration and invasion were assessed using uncoated and Matrigel-coated 8-μm-pore inserts, respectively (cat. no. 725301; Wuxi NEST Biotechnology Co., Ltd.). For invasion assays, inserts were coated with 50 μl Matrigel (cat. no. 354234; Corning, Inc.) diluted 1:6 in prechilled serum-free medium and incubated at 37˚C for 1 h. At 24 h after transfection, SK-MEL-28 and A375 cells were seeded into the upper chambers at $2x10^4$ cells/chamber in 200 μl serum-free medium. For drug-treatment experiments, the upper medium contained 10 μM methapyrilene or an equivalent volume of DMSO. The final DMSO concentration was 0.1% (v/v) in all groups. The lower chambers contained 500 μl medium supplemented with 10% FBS. Following incubation at 37˚C with 5% CO_2 for 48 h, cells remaining on the upper membrane surface were removed with a cotton swab. Cells on the lower surface were fixed with 4% paraformaldehyde and stained with 0.1% (w/v) crystal violet for 15-30 min each at room temperature. Membranes were rinsed and air-dried, and images were captured using an inverted light microscope in bright-field mode (ICX41; Ningbo Sunny Instruments Co., Ltd.).

Western blotting analysis. SK-MEL-28 and A375 cells following the indicated transfection or drug treatments were washed once with ice-cold PBS and lysed on ice for 30 min using RIPA buffer (cat. no. PMK0211; Hubei Bioprimacy Biotechnology Co., Ltd.) containing protease and phosphatase inhibitors. Lysates were centrifuged at 12,000 x g for 15 min at 4˚C, and the supernatants were collected. Protein concentrations were quantified using a BCA assay (cat. no. P0010; Beyotime Biotechnology). Equal amounts of protein (20 μg/lane) were separated on 6% gels using SDS-PAGE (cat. no. G2175; Wuhan Servicebio Technology Co., Ltd.), and transferred to PVDF membranes (cat. no. IPVH00010; Merck KGaA). Membranes were blocked with 5% (w/v) non-fat milk in TBST (cat. no. T1085; Beijing Solarbio Science & Technology Co., Ltd.) for 1 h at room temperature and incubated overnight at 4˚C with primary antibodies against BPTF (1:1,000; cat. no. Z33292; Beijing Bio-Lab Technology Co., Ltd.), p53 (1:1,000; cat. no. bs-8687R; BIOSS), phosphorylated (p)-p53 [serine (Ser)15; 1:500; cat. no. bs-3702R; BIOSS)], p21 (1:2,000; cat. no. HA724295; Hangzhou HuaAn Biotechnology Co., Ltd.), MDM2 (1:1,000; cat. no. 27883-1-AP; Proteintech Group, Inc.), PD-L1 (1:1,000; cat. no. R30023; ZENBIO Co., Ltd.) and β-actin (1:20,000; cat. no. 66009-1-Ig; Proteintech Group, Inc.). Membranes were subsequently incubated for 1 h at room temperature with HRP-conjugated goat anti-mouse IgG H&L (1:5,000; cat. no. 511103; ZENBIO Co., Ltd.) or Goat Anti-Rabbit IgG H&L (1:2,000; cat. no. 511203; ZENBIO Co., Ltd.). Protein bands were visualized using an enhanced chemiluminescence reagent (cat. no. PMK0666; Hubei Bioprimacy Biotechnology Co., Ltd.) with a substrate incubation time of 1-3 min and imaged using a Tanon 5200T chemiluminescence imaging system. Band intensities were quantified using ImageJ software (version 1.54g; National Institutes of Health). Target protein levels were normalized to β-actin, whereas p-p53(Ser15) levels were normalized to total p53.

Reciprocal co-immunoprecipitation (co-IP) assay. Co-IP was performed in untreated SK-MEL-28 and A375 cells. Cells were seeded at $1x10^6$ cells/100-mm dish and cultured at 37˚C with 5% CO_2 to 70-80% confluence. Cells were lysed in Pierce IP Lysis Buffer (cat. no. 87787; Thermo Fisher Scientific, Inc.), supplemented with Halt Protease and Phosphatase Inhibitor Cocktail (cat. no. 78440; Thermo Fisher Scientific, Inc.) at 1:100 immediately before use. An aliquot of each lysate was retained as the input control. Equal amounts of protein (0.5-1.0 mg/reaction in a total volume of 400-500 μl) were incubated overnight at 4˚C with anti-BPTF (2 μg/mg total protein; cat. no. ab72036; Abcam), anti-p53 (2 μg/reaction; cat. no. ab1101; Abcam) or matched IgG antibodies (Rabbit polyclonal IgG; cat. no. ab171870; Abcam) and mouse IgG2a κ [MOPC-173] (cat. no. ab18413; Abcam). Immune complexes were captured using 20 μl Protein A+G magnetic bead suspension per reaction from an Immunoprecipitation Kit with Protein A+G Magnetic Beads (cat. no. P2179S; Beyotime Biotechnology). Beads were washed three times with 500 μl 1X TBS prepared from the kit-supplied 10X TBS. Following centrifugation 3,000 x g for 2 min at 4˚C and magnetic separation, bead-bound proteins were eluted in 2X SDS sample buffer containing β-mercaptoethanol at 95-100˚C for 5-10 min. Eluates were collected by magnetic separation and analyzed alongside input samples by western blotting for BPTF and p53, using the aforementioned protocol.

Chromatin immunoprecipitation (ChIP). ChIP-quantitative PCR (qPCR) was performed separately in vector vs. BPTF-OE cells and shNC vs. shBPTF cells. Cells were cross-linked with 1% formaldehyde, and chromatin was sonicated at 20 kHz and high power in a 4˚C water bath for 20 cycles of 30 sec ON/30 sec OFF. An aliquot was reverse-cross-linked, treated with RNase A and proteinase K, and purified for fragment-size assessment (200-500 bp) by 1.5% agarose gel electrophoresis alongside a 100-bp DNA ladder. A 1% aliquot of the sonicated chromatin was retained before immunoprecipitation as the input control. Equal amounts of chromatin (10-20 μg/reaction) were immunoprecipitated with a ChIP-validated anti-BPTF antibody (cat. no. ABE1966; Sigma-Aldrich; Merck KGaA) antibody or matched IgG, with an aliquot retained as input. ChIP and input DNA was purified using a ChIP DNA Clean and Concentrator kit (cat. no. D5201; Zymo Research Corporation). qPCR was performed using Universal Blue SYBR Green qPCR Master Mix (cat. no. G3326-05; Wuhan Servicebio Technology Co., Ltd.), with primers targeting the predicted BPTF-binding regions within the *TP53* and *CD274* promoters.

Cycling conditions were 95˚C for 30 sec, followed by 40 cycles of 95˚C for 15 sec, 60˚C for 15 sec and 60˚C for 30 sec. Data were analyzed using SLAN software (version 8.2.2; Shanghai Hongshi Medical Technology Co., Ltd.). Enrichment was calculated using the percent input method, as % input=100 $x2^{(Cq_adjusted\ input-Cq_IP)}$, where Cq_adjusted input=Cq_1% input-$\log_2(100)$. The primer sequences used were as follows: *CD274* forward (F), 5'-CATATGGGTCTGCTGCTGAC-3' and reverse (R), 5'-CAACAAGCCAACATCTGAAC-3'; *TP53* F, 5'-TATCTACGGCACCAGGTCGG-3' and R, 5'-AGTAAG GGCAAGTAATCCGCC-3'; and *GAPDH* F, 5'-TACTAGCGG TTTTACGGGCG-3' and R, 5'-TCGAACAGGAGGAGCAGA GAGCGA-3'.

Dual-luciferase reporter assay. The predicted BPTF-responsive promoter regions of *TP53* and *CD274* promoters were cloned separately into the promoterless pGL4.10[luc2] firefly luciferase vector (cat. no. E6651; Promega Corporation). SK-MEL-28 and A375 cells were co-transfected with the corresponding promoter reporter, the pGL4.74[hRluc/TK] *Renilla* control vector (cat. no. E6921; Promega Corporation) and BPTF-OE, shBPTF or the respective matched control constructs using Lipofectamine 3000 (cat. no. L3000015; Invitrogen; Thermo Fisher Scientific, Inc.). Promoter activity was evaluated separately in vector vs. BPTF-OE cells and in shNC vs. shBPTF cells. At 48 h post-transfection, luciferase activities were measured using the Dual-Luciferase® Reporter Assay System (cat. no. E1910; Promega Corporation), and firefly luciferase activity was normalized to *Renilla* luciferase activity.

Cellular thermal shift assay (CETSA). SK-MEL-28 and A375 cells seeded at $1x10^6$ cells/100-mm dish in DMEM supplemented with 10% FBS and cultured at 37˚C with 5% CO_2 to 80-90% confluence. Cells were treated with 10 μM methapyrilene or an equivalent volume of DMSO for 48 h, harvested and resuspended in ice-cold PBS containing protease inhibitors at ~$1x10^7$ cells/ml. The suspension was distributed into PCR tubes (100 μl/tube; ~$1x10^6$ cells). Equal aliquots were heated at 42, 46, 50, 54, 58, 62, 66 or 70˚C for 3 min, followed by cooling at 4˚C for 3 min. Cells were lysed by three freeze-thaw cycles using liquid nitrogen and a 25˚C water bath. Lysates were centrifuged at 20,000 x g for 20 min at 4˚C, and supernatants were transferred to prechilled tubes. Soluble fractions were analyzed by western blotting using the BPTF antibody (1:1,000; cat. no. Z33292; Beijing Bio-Lab Technology Co., Ltd.) with antibody incubation and detection conditions as aforementioned. BPTF band intensities were normalized within each treatment group to the signal at 42˚C, which was set to 1. Relative soluble BPTF levels at the remaining temperatures were calculated accordingly. Thermal denaturation curves were fitted by non-linear regression, and apparent melting temperatures were estimated from the fitted curves.

Drug affinity-responsive target stability (DARTS) assay. SK-MEL-28 cells were seeded at $1x10^6$ cells per 100-mm dish and cultured in DMEM supplemented with 10% FBS at 37˚C with 5% CO_2 until 80-90% confluent. Cells were washed twice with ice-cold PBS and lysed on ice for 30 min in Pierce IP Lysis Buffer (cat. no. 87787; Thermo Fisher Scientific, Inc.) supplemented with protease and phosphatase inhibitors. Lysates were centrifuged at 20,000 x g for 20 min at 4˚C, and supernatant protein concentrations were determined using a BCA assay. Native lysates (20 μg total protein per reaction) from SK-MEL-28 cells were pre-incubated with 10 μM methapyrilene or an equivalent volume of DMSO on ice for 1 h, followed by 30 min at room temperature. Limited proteolysis was performed with Pronase® (cat. no. 53702; Sigma-Aldrich; Merck KGaA), freshly prepared in digestion buffer, at enzyme-to-total-protein ratios of 1:1,000, 1:500 and 1:200 (w/w) for 15 min at 35˚C. Parallel samples without Pronase® were included as undigested controls. Proteolysis was terminated by the addition of SDS loading buffer (cat. no. G2031; Wuhan Servicebio Technology Co., Ltd.), followed immediately by heating at 95-100˚C for 3-5 min. Residual BPTF was detected by western blotting using the antibody incubation and detection conditions aforementioned. BPTF abundance was normalized to the corresponding undigested control.

T-cell cytotoxicity assay. $CD8^+$ T cells were isolated from healthy donor peripheral blood mononuclear cells commercially obtained from Sichuan Bio Biotechnology Co., Ltd. (cat. no. B26919; http://htycbio.com/gaozhiliangxibaoku/202608/1058.html) using the $CD8^+$ T Cell Isolation Kit (cat. no. 130-096-495; Miltenyi Biotec GmbH). The purity of $CD8^+$ T cells was confirmed using flow cytometry (>95%) using FITC Plus-conjugated anti-CD3 (cat. no. FITC-65133; Proteintech Group, Inc.) and PE-conjugated anti-CD8 (cat. no. PE-65559; Proteintech Group, Inc.) antibodies; each at 5 μl per 10^6 cells in a 100-μl suspension. For activation, flat-bottom 96-well plates were coated with 50 μl/well anti-human CD3 antibody (5 μg/ml; cat. no. 65133-1-Ig; Proteintech Group, Inc.) overnight at 4˚C and washed with sterile PBS. T cells were seeded at $1-2x10^6$ cells/ml (100 μl/well) in complete RPMI-1640 medium and activated for 3 days at 37˚C with 5% CO_2 in the presence of soluble anti-human CD28 antibody (2 μg/ml; cat. no. 65099-1-Ig; Proteintech Group, Inc.) and recombinant human IL-2 (30 U/ml; cat. no. PB180634; Procell Life Science & Technology Co., Ltd.). Activated T cells were co-cultured with SK-MEL-28 or A375 cells at an effector-to-target ratio of 10:1 ($1x10^5$ T cells and $1x10^4$ target cells per well) for 6 h at 37˚C in an incubator containing 5% CO_2. Cytotoxicity was quantified using a lactate dehydrogenase (LDH) release assay (cat. no. C0016; Beyotime Biotechnology Co., Ltd.).

Flow cytometric analysis of $CD8^+$ T-cell function. After 18 h of co-culture with SK-MEL-28 cells, T cells were harvested by gentle pipetting, and the culture supernatant was combined with a single ice-cold PBS rinse of each well. Cells were centrifuged at 300 x g for 10 min at 4˚C, washed once with ice-cold PBS and resuspended in 100 μl PBS. Fc receptors were blocked using 1 μl MonoZero® Human Fc Blocking Reagent (cat. no. PF00032; Proteintech Group, Inc.) for 10 min at room temperature. Cells were stained at 4˚C in the dark with 7-aminoactinomycin D (5 μl/10^6 cells; cat. no. PD00101; Proteintech Group, Inc.) for 10 min, followed by PE-conjugated anti-CD8 (cat. no. PE-FcA65630; Proteintech Group, Inc.), FITC Plus-conjugated anti-CD69 (cat. no. FITC-98173; Proteintech Group, Inc.) and APC-conjugated anti-programmed cell death protein-1 (PD-1; cat. no. APC-65586; Proteintech Group, Inc.), each at 5 μl/10^6 cells, for 30 min.

For intracellular IFN-γ detection, 10^6 cells were fixed and permeabilized with 500 μl Fix/Perm Buffer from the Intracellular Flow Cytometry Fixation & Permeabilization

Buffer Kit (cat. no. PF00019; Proteintech Group, Inc.) for 15 min at room temperature in the dark. After two washes with 1X Perm/Wash Buffer, cells were resuspended in 100 μl of the same buffer and stained with 5 μl FITC Plus-conjugated anti-IFN-γ (cat. no. FITC-98187; Proteintech Group, Inc.) for 30 min at 4˚C in the dark. Cells were washed twice and resuspended in 200 μl 1X Perm/Wash Buffer. Flow cytometry data were acquired using a FongCyte C2060 flow cytometer (Beijing Challen Biotechnology Co., Ltd.) and analyzed using FlowJo software (version 10.8; BD Biosciences). Positive gates were defined using negative controls and fluorescence-minus-one controls for CD69, IFN-γ and PD-1. $CD69^+CD8^+$, $IFN\text{-}\gamma^+CD8^+$ and $PD\text{-}1^+CD8^+$ populations were quantified, and PD-1 mean fluorescence intensity (MFI) was calculated within viable $CD3^+CD8^+$ T cells.

PD-L1 blockade experiment. SK-MEL-28 cells were seeded at $8x10^3$ cells/well in 96-well plates and allowed to adhere overnight before adding $CD8^+$ T cells at an effector-to-target ratio of 10:1 ($8x10^4$ T cells/well). Co-cultures were treated with 10 μM methapyrilene, 10 μg/ml anti-PD-L1 antibody (clone MIH1; cat. no. 16-5983-82; Thermo Fisher Scientific, Inc.), or a combination of the two treatments or the corresponding vehicle and isotype controls for 48 h at 37˚C with 5% CO_2. Control cultures received an equivalent volume of DMSO and 10 μg/ml mouse IgG1 isotype control antibody (cat. no. 14-4714; Thermo Fisher Scientific, Inc.). After incubation, plates were centrifuged at 200-400 x g for 10 min at room temperature, and supernatants were collected. LDH activity was measured using the LDH release assay (cat. no. C0016; Beyotime Biotechnology). Levels of IFN-γ (cat. no. JL12152; Shanghai Future Industrial Co., Ltd.) and granzyme B (cat. no. EK158; MultiSciences (Lianke) Biotech Co., Ltd.) were determined using ELISA kits according to the manufacturers' protocols.

Flow-cytometric detection of tumor-cell surface PD-L1. Tumor cells subjected to different treatments were stained with a phycoerythrin-conjugated anti-PD-L1/CD274 antibody (cat. no. PE-98062; Proteintech Group, Inc.) at 5 μl/10^6 cells for 30 min at 4˚C in the dark. Surface PD-L1 expression levels were quantified in viable, singlet tumor cells using flow cytometry and analysis software aforementioned, and reported as both the percentage of $PD\text{-}L1^+$ cells and PD-L1 MFI.

Statistical analysis. All statistical analyses were performed in R software (version 4.3.0; Posit Software, PBC). Comparisons between two groups were conducted using an unpaired, two-tailed Student's t-test or the Mann-Whitney U test, as appropriate. Multigroup and factorial experiments were analyzed using one- or two-way ANOVA, both followed by Tukey's post hoc test. Benjamini-Hochberg correction was applied to high-dimensional multiple testing. All tests were two-sided and $P<0.05$ was considered to indicate a statistically significant difference. All *in vitro* experiments were performed in triplicate and data are presented as the mean ± SEM.

Results

Transcriptomic integration identifies genes associated with immunotherapy non-response. To identify genes associated with immunotherapy response, the transcriptomic data from four melanoma datasets (dataset nos. GSE91061, phs000452, PRJEB23709 and GSE122220) were integrated. PCA demonstrated that, before batch correction, samples clustered primarily by dataset of origin rather than by immunotherapy response status (Fig. 1A). 'ComBat' correction attenuated dataset-associated clustering across the first two principal components and made response-associated separation more apparent (Fig. 1B). Differential expression analysis identified 453 genes differentially expressed between immunotherapy non-responders and responders. These genes comprised 209 upregulated and 244 downregulated genes in non-responders ($P<0.05$ and $\log_2FC>0.25$; Fig. 1C and D). To identify potentially actionable transcriptional regulators associated with immunotherapy non-response, a directionally constrained discovery strategy was adopted that prioritized genes upregulated in non-responders. The downregulated genes were not considered biologically irrelevant but were not carried forward within the predefined inhibitory target-discovery framework.

Numerous ML algorithms refine the candidate set. To limit dependence on a single feature-selection framework, three ML algorithms (LASSO, SVM-RFE and RF), were used to screen the 209 genes upregulated in non-responders. These algorithms captured complementary selection principles based on coefficient shrinkage, recursive margin-based feature elimination and non-linear ensemble-based feature importance, respectively. LASSO retained 36 genes with non-zero coefficients at the penalty parameter (λ.min) that minimized the CV error (Fig. 2A and B). SVM-RFE achieved the highest 10-fold CV performance with seven genes, yielding the lowest error of 0.326 and a corresponding accuracy of 0.674 (Fig. 2C and D). In the RF analysis, the OOB error stabilized as the number of trees increased. A total of 41 genes were identified, including ZNF462, YWHAE and IL13RA2 (Fig. 2E and F). These algorithm-specific results provided a preliminary set of candidate genes.

Cross-model analysis prioritizes BPTF. To identify features that were robust to the choice of algorithm, the LASSO, SVM-RFE and RF outputs were intersected. A total of six genes were identified: CHD7 (chr8), ZNF462 (chr9), PMP22 (chr17), WNK4 (chr17), BPTF (chr17) and TXN2 (chr22) (Fig. 3A and B). Subsequently eight ML models were constructed using the six-gene feature set. Among these models, the GBM model achieved the highest AUC of 0.741 (Fig. 3C). SHAP analysis of the GBM model assigned the highest mean absolute SHAP value to BPTF, followed by ZNF462, CHD7, WNK4, TXN2 and PMP22 (Fig. 3D). Across all eight models, BPTF ranked first in six models and second in the remaining two, indicating consistent model-based importance across distinct analytical frameworks (Table SV). SHAP dependence analysis further demonstrated a non-linear relationship between feature expression and model output (Fig. 3E). The transition from positive to negative SHAP values as BPTF expression increase indicated a lower predicted response probability. Therefore, these cross-model results prioritized BPTF for subsequent mechanistic investigation.

BPTF promotes malignant phenotypes and regulates p53/PD-L1 signaling. To characterize the biological programs associated with BPTF expression and identify candidate

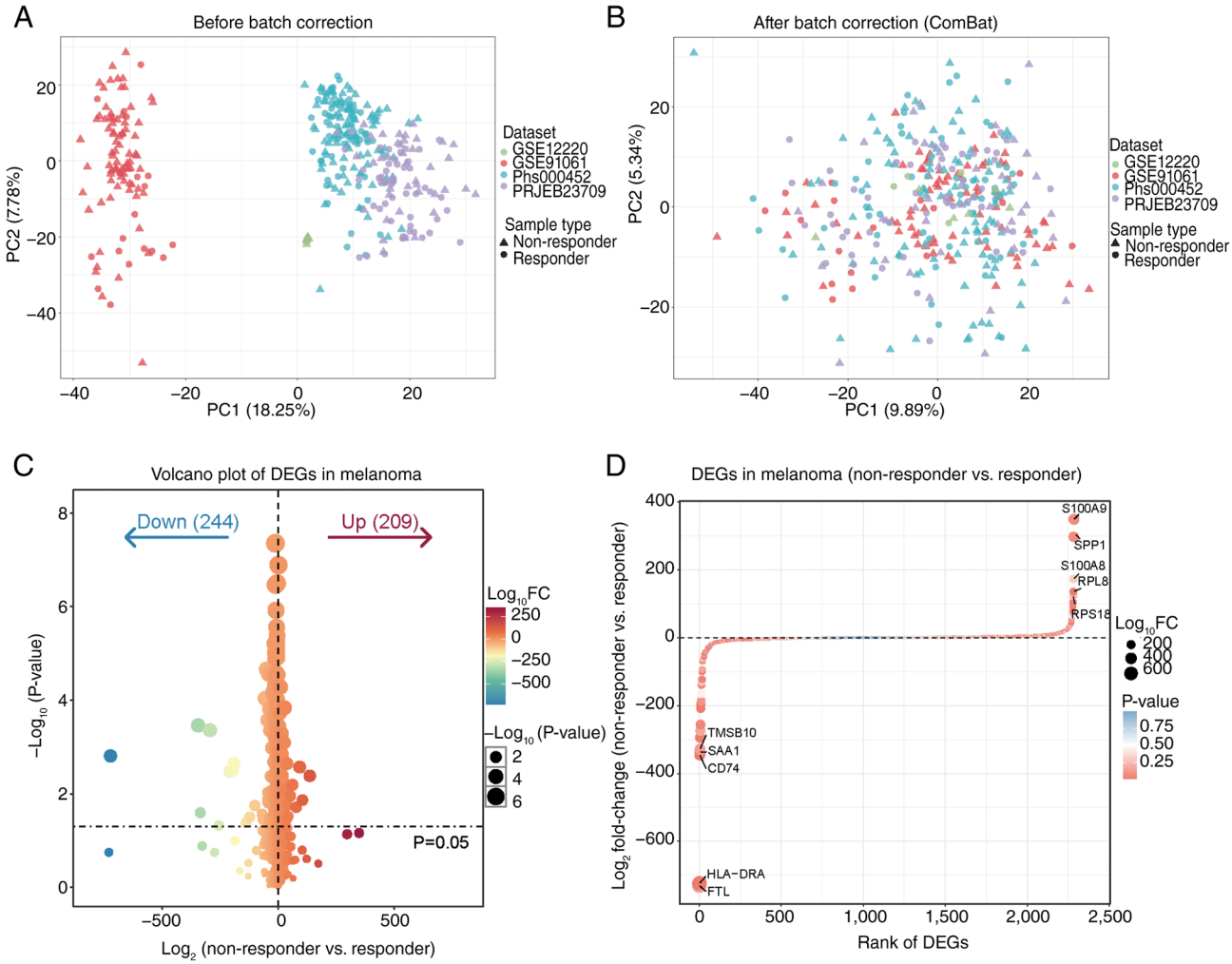


Figure 1. Data integration and differential gene expression analysis in melanoma immunotherapy response. (A) PC analysis before batch correction. Each point represents one sample, with color indicating the dataset of origin and shape indicating response status (circle, responder; triangle, non-responder). (B) PC analysis after batch correction. Each point represents one sample, with color indicating the dataset of origin and shape indicating response status (circle, responder; triangle, non-responder). (C) Volcano plot of differential gene expression between the non-responder and responder groups. The x-axis indicates log_2FC and the y-axis indicates-log_{10}(P-value). Genes displayed using a color gradient from blue (downregulated) to red (upregulated). The vertical dashed lines indicate the log_2FC>0.25 threshold and the horizontal dashed line indicates the P<0.05 threshold. Numbers in brackets indicate the number of significantly upregulated and downregulated genes. (D) Gene expression ranking plot. All genes are ordered according from the lowest to the highest log_2FC values. Points are colored based on the P-value magnitude and sized based on the absolute log_2FC value. The top five upregulated and bottom five downregulated genes are labeled. FC, fold-change; PC, principal component; DEGs, differentially expressed gene.

mechanisms, KEGG and Hallmark pathway enrichment analyses were performed. KEGG analysis revealed positive enrichment of 'ubiquitin-mediated proteolysis', 'cell cycle' and 'endometrial cancer' pathways in BPTF-high samples. 'Glutathione metabolism', 'amino sugar and nucleotide sugar metabolism' and 'porphyrin and chlorophyll metabolism' were negatively enriched (Fig. 4A). Hallmark analysis similarly identified positive enrichment of 'Myc targets V1', 'E2F targets' and 'G_2M checkpoint'. The 'p53 pathway', 'hypoxia' and 'IL2-STAT5 signaling' were negatively enriched (Fig. 4B). Among these pathways, the p53 pathway was selected for hypothesis-driven follow-up due to its established roles in melanoma cell-cycle control and PD-L1 regulation (33,34).

To determine the functional effects of BPTF regulation, gain- and loss-of-function experiments were performed in SK-MEL-28 and A375 cells. BPTF overexpression significantly enhanced colony formation, migratory and invasive abilities, whereas BPTF knockdown significantly reduced these malignant phenotypes (all P<0.05; Figs. 4C and D and S1A and B). Western blotting demonstrated that BPTF overexpression significantly decreased the expression levels of p53 and p21 but significantly increased the expression levels of MDM2 and PD-L1. By contrast, BPTF knockdown produced the opposite expression pattern (Figs. 4E and S1C). The p-p53(Ser15)/p53 ratio was not significantly altered by either BPTF overexpression or knockdown. The two shRNAs produced similar phenotypic and molecular effects; therefore, shBPTF-1 was randomly chosen for use in subsequent experiments. These effects were reproduced in SK-MEL-2 and MeWo cells, in which BPTF overexpression significantly enhanced clonogenic growth, suppressed p53 and p21 expression, and increased MDM2 and PD-L1 expression (Fig. S2).

The molecular relationship was investigated between BPTF and the p53/PD-L1 axis. Reciprocal co-IP confirmed the BPTF-p53 interaction in both SK-MEL-28 and A375

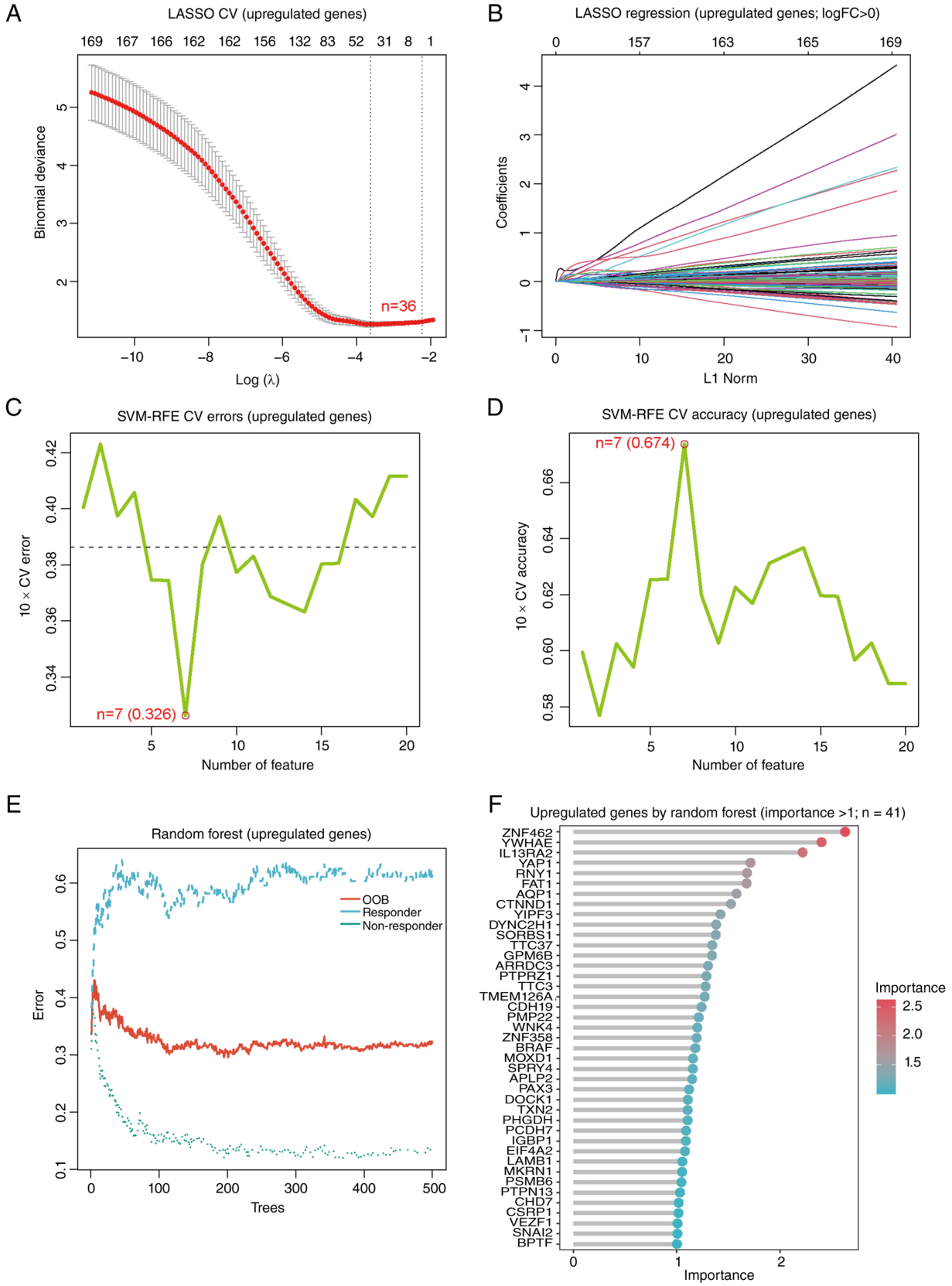


Figure 2. Machine-learning-based feature selection for immune escape genes. (A) LASSO CV plot. The left vertical dashed line indicates λ.min, and the right vertical dashed indicates λ.1se. Numbers at the top indicate the number of variables selected at each λ value. At λ.min, 36 feature genes were selected. (B) LASSO regression coefficient profile. Each colored line represents a different gene, and the trajectory indicates when genes enter (coefficient becomes non-zero) or exit (coefficient becomes zero) the model. (C) SVM-RFE CV error. (D) SVM-RFE CV accuracy. (E) Random forest OOB rate plot. The red curve indicates the overall classification error rate and the number as a function of the number of trees, while the blue and green curves represent the class-specific error rates for the responder and non-responder groups, respectively. (F) Random forest feature importance dot plot. Genes are ranked by importance and colored by their importance scores. Only genes with importance >1 are displayed as selected features (n=41). LASSO, least absolute shrinkage and selection operator; SVM-RFE, support vector machine-recursive feature elimination; CV, cross-validation; OOB, out-of-bag; λ.min, minimum error; λ.1se, one standard error rule.

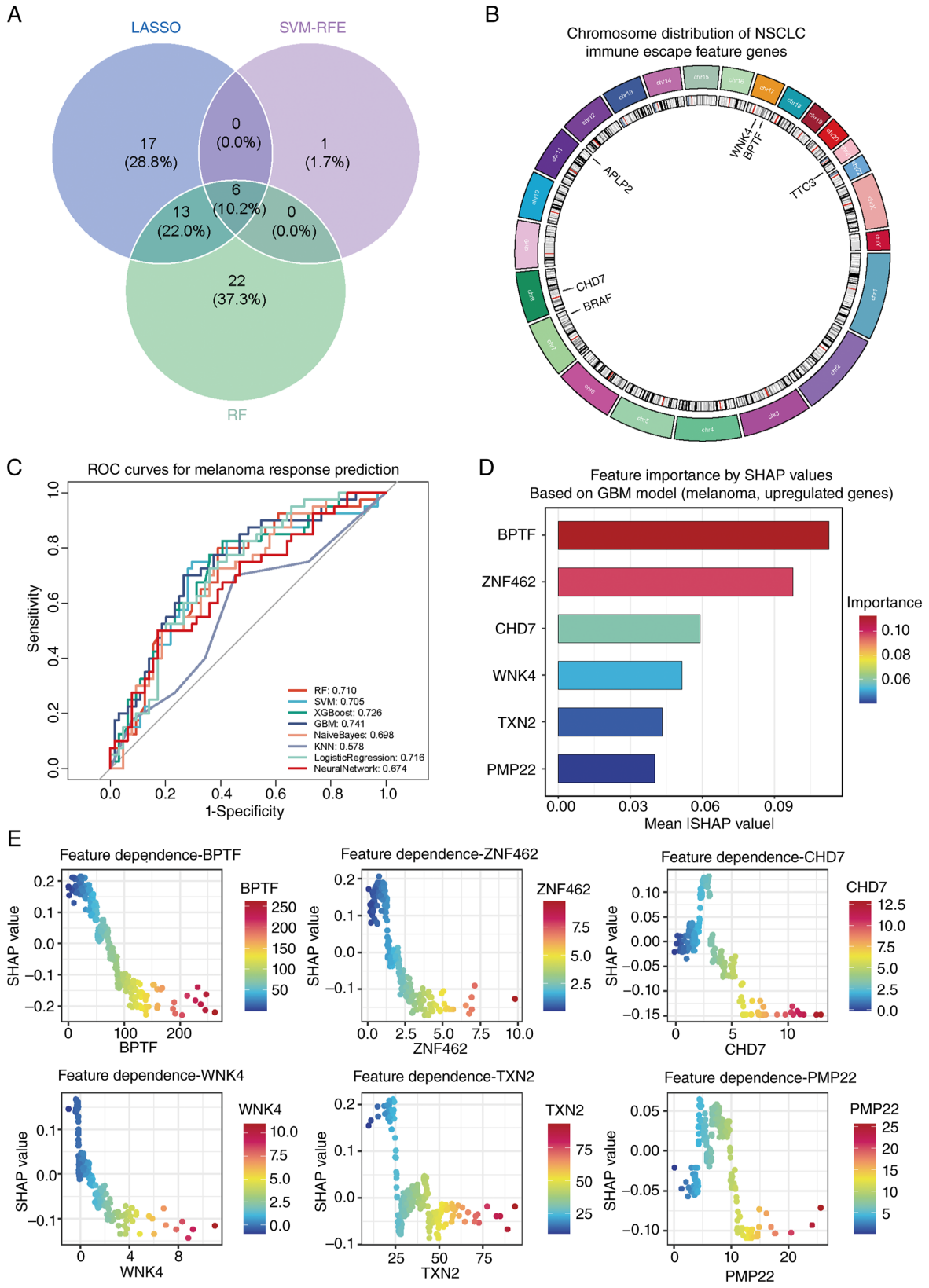


Figure 3. Characteristic gene integration and interpretation analysis. (A) Venn diagram of genes selected by the three machine-learning methods. Values within the Venn diagram indicate the number of genes unique to each method or shared among methods. The intersection represents the final consensus feature genes. (B) Chromosomal distribution of the selected feature genes. Each chromosome is represented as a colored segment with gene positions marked. (C) ROC curves for the eight machine-learning models. Each curve is presented in a different color, with the corresponding area under the curve values listed in the key. (D) SHAP feature importance bar plot from the best-performing model. Features are ranked from the most to the least important, with bar colors indicating the magnitude of feature importance. (E) SHAP dependence plots. The x-axis represents feature gene values and the y-axis represents SHAP values. Point colors indicate feature-value magnitude and demonstrate the contribution of each feature to model predictions. SHAP, SHapley Additive exPlanations; LASSO, least absolute shrinkage and selection operator; SVM-RFE, support vector machine-recursive feature elimination; ROC, receiver operating characteristic; RF, random forest; GBM, gradient boosting machine; KNN, K-nearest neighbors; BPTF, bromodomain plant homeodomain finger transcription factor; chr, chromosome.

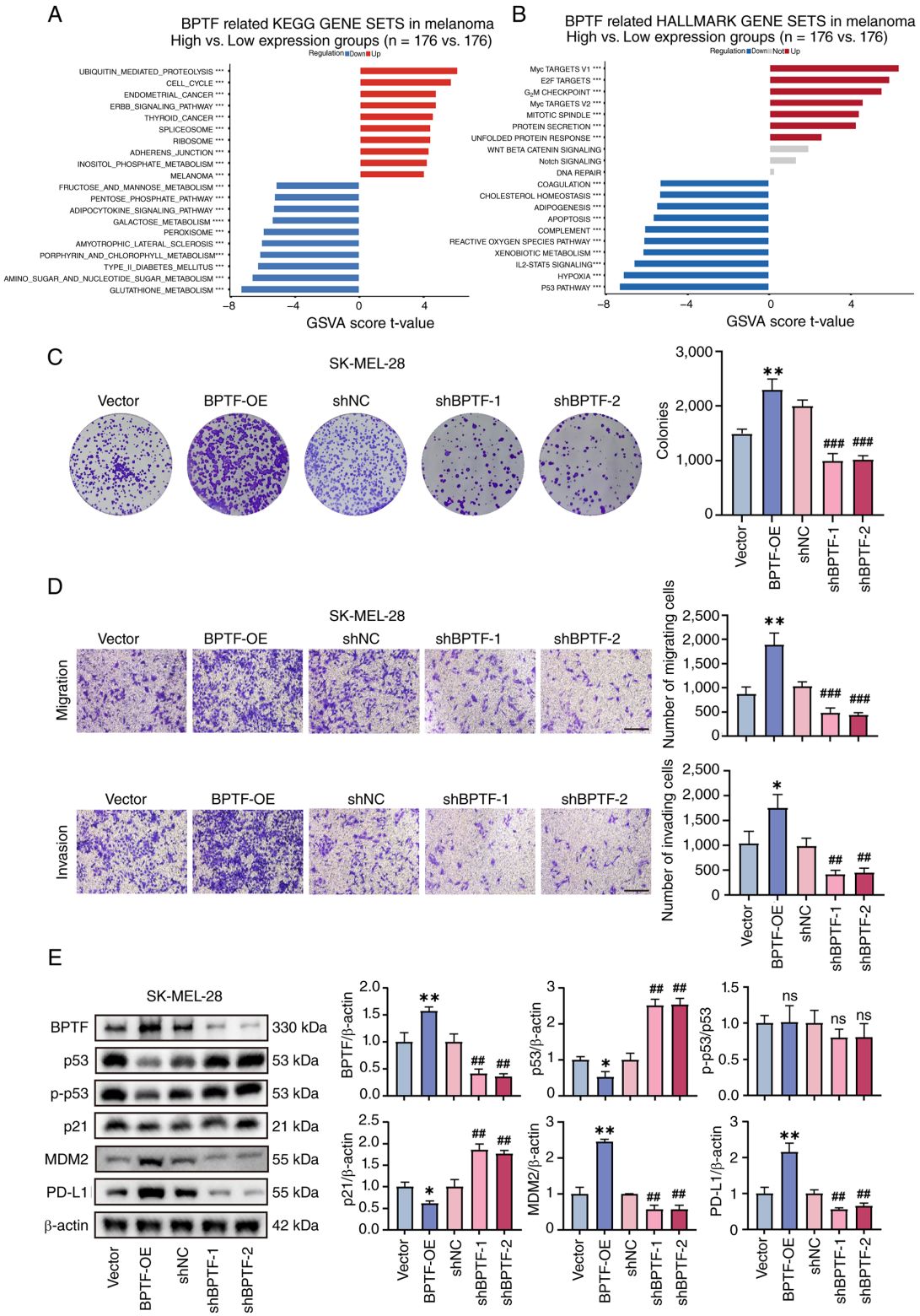


Figure 4. Functional pathway analysis and experimental validation of BPTF in SK-MEL-28 cells. (A) KEGG pathway enrichment (BPTF-high vs. BPTF-low groups). Bars are colored by the direction of regulation: Red for upregulated pathways and blue for downregulated pathways. Pathway names are followed by significance indicators (***P<0.001). (B) Hallmark pathway enrichment (BPTF-high vs. BPTF-low groups). Bars are colored by the regulation direction: Red for upregulated pathways; blue for downregulated pathways; and grey bars indicate no statistically significant difference between groups. Pathway names are followed by significance indicators (***P<0.001). (C) Colony formation assay in SK-MEL-28 cells following BPTF overexpression or knockdown. Bar graphs indicate relative colony numbers (vs. vector, **P<0.01; vs. shNC, $^{###}$P<0.001). (D) Cell migration assay in SK-MEL-28 cells following BPTF overexpression or knockdown. Bar graphs show the numbers of migrating and invading cells (vs. vector, *P<0.05 and **P<0.01; vs. shNC, $^{##}$P<0.01 and $^{###}$P<0.001). Magnification, x100; scale bars, 200 μm. (E) Representative western blots and semi-quantitative analysis of proteins in p53/PD-L1 axis following BPTF overexpression or knockdown in SK-MEL-28 cells. p-p53 (serine 15) was quantified relative to total p53, whereas the other proteins were normalized to β-actin. Bar graphs indicate protein-expression levels compared with the corresponding control (vs. vector, *P<0.05 and **P<0.01; vs. shNC, $^{##}$P<0.01). BPTF, bromodomain plant homeodomain finger transcription factor; KEGG, Kyoto Encyclopedia of Genes and Genomes; NC, negative control; BPTF-OE, BPTF-overexpressed; PD-L1, programmed death-ligand 1; p-p53, phosphorylated p53; shNC, non-targeting short hairpin RNA control; shBPTF, BPTF knockdown; MDM2, mouse double minute 2.

cells (Fig. S3A and B). ChIP-qPCR further demonstrated the occupancy of BPTF at the TP53 and CD274 promoter regions. BPTF overexpression increased occupancy at both regions, whereas BPTF knockdown reduced it (all P<0.01; Fig. S3C). In dual-luciferase reporter assays, BPTF overexpression reduced TP53 promoter activity and increased CD274 promoter activity, while BPTF knockdown produced the opposite effects (all P<0.01; Fig. S3D). BPTF-mediated TP53 repression may therefore reduce both total and phosphorylated p53 abundance, consistent with the stable phosphorylation ratio. Therefore, these findings support coordinated transcriptional regulation of TP53 and CD274 by BPTF.

Drug-gene analysis prioritizes methapyrilene. To identify compounds associated with the six candidate genes, drug-gene interaction analysis was performed. Enrichment analysis highlighted several significant drugs associations, including ketoprofen, *Cochliobolus carbonum* (HC toxin), tyrphostin AG-825, ritodrine, (+)-isoprenaline, clenbuterol, methapyrilene and AG-012559 (P<0.05; Fig. 5A). The drug-gene interaction network demonstrated that BPTF interacted with both regulatory drugs (HC toxin) and inhibitory drugs (tyrphostin AG-825 and methapyrilene) and was also associated with CHD7 (Fig. 5B). However, tyrphostin AG-825 was associated with both CHD7 and BPTF, while methapyrilene was associated only to BPTF. Therefore, methapyrilene was prioritized for further validation in the present study.

Molecular docking predicted methapyrilene binding to BPTF with a Vina score of -6.2 kcal/mol (Fig. 5C). The predicted pocket comprised Trp2824, Pro2825, Phe2826, Leu2827, Glu2828, Pro2829, Val2830 and Asp2831 in chain A. During the 100-nsec molecular dynamics simulation, the BPTF-methapyrilene complex remained conformationally stable and exhibited lower global and residue-level fluctuations compared with apo BPTF. The MM/GBSA-estimated binding free energy of BPTF-methapyrilene was similar to that of the reference BPTF ligand AU1 (Fig. 5D). CETSA further demonstrated methapyrilene-induced rightward shifts in the thermal melting curves of endogenous BPTF, with increases in apparent melting temperature of 5.21˚C in SK-MEL-28 cells and 4.19˚C in A375 cells (Fig. 5E and F). Consistently, DARTS revealed that methapyrilene increased BPTF resistance to proteolytic degradation in SK-MEL-28 cells (all P<0.05; Fig. 5G). Therefore, these results support an interaction between methapyrilene and BPTF.

Methapyrilene counteracts BPTF-mediated melanoma phenotypes. To verify the ability of methapyrilene to counteract BPTF function, its activity was evaluated in BPTF gain- and loss-of-function models. In SK-MEL-28 and A375 cells, methapyrilene significantly reduced basal clonogenic growth and invasion, and attenuated the increases induced by BPTF overexpression (all P<0.05; Figs. 6A and B and S4A and B). BPTF knockdown, methapyrilene treatment and their combination each suppressed clonogenic growth and invasion (all P<0.05). However, the combination produced no significant additional suppression compared with BPTF knockdown alone (Figs. 6A and B and S4A and B).

Western blotting revealed that methapyrilene significantly increased the expression levels of p53, p-p53(Ser15) and p21, while decreasing the expression levels of MDM2 and PD-L1 in SK-MEL-28 and A375 cells (all P<0.05). The p-p53(Ser15)/p53 ratio was not significantly altered among the treatment groups. While BPTF overexpression produced the reciprocal pattern, methapyrilene significantly reversed these changes without reducing the elevated BPTF protein abundance (all P<0.05). BPTF knockdown and methapyrilene treatment each activated p53-associated signaling and reduced MDM2 and PD-L1 expression (all P<0.05), whereas their combination further increased p53 and p21 expression and decreased MDM2 and PD-L1 expression compared with BPTF knockdown alone (all P<0.05; Figs. 6C and S4C). Therefore, these findings indicated that methapyrilene attenuates BPTF-associated malignant phenotypes and restores dysregulated MDM2/p53/PD-L1 signaling. These non-additive phenotypic and molecular effects support an at least partially BPTF-dependent component of methapyrilene activity.

Methapyrilene partially reverses BPTF-mediated suppression of T-cell function. To further elucidate the mechanism of BPTF-mediated immune evasion, an *in vitro* T cell-tumor cell co-culture system was established. In both the SK-MEL-28 and A375 co-culture models, BPTF overexpression reduced T-cell-mediated tumor cell lysis measured by LDH release, whereas methapyrilene partially restored tumor cell killing (all P<0.001; Fig. 7A). By contrast, BPTF knockdown increased T-cell-mediated killing in both models (all P<0.05; Fig. S5A). These reciprocal perturbations identify tumor cell BPTF as a negative regulator of T-cell-mediated cytotoxicity.

The $CD8^+$ T cell phenotype underlying the altered tumor cell killing was characterized. In the SK-MEL-28 co-culture system, BPTF overexpression reduced the proportions of $CD69^+CD8^+$ and IFN-γ^+CD8^+ T cell populations (all P<0.001; Fig. 7B). BPTF overexpression concurrently increased the proportion of PD-1^+CD8^+ T cells and the MFI of PD-1 within the $CD8^+$ T cell population (all P<0.001). Methapyrilene partially reversed these changes (all P<0.05) (Fig. 7C). BPTF knockdown produced the reciprocal phenotype, and methapyrilene further accentuated these changes in BPTF-knockdown co-cultures (all P<0.05; Fig. S5B and C).

Functionally, PD-L1 blockade increased T-cell-mediated tumor cell killing to a level similar to that achieved with methapyrilene alone. Combining methapyrilene with PD-L1 blockade further increased tumor-cell killing (P<0.0001; Fig. 7D). Secreted effector molecules exhibited a consistent pattern. BPTF overexpression reduced the secretion of IFN-γ and granzyme B. Methapyrilene or PD-L1 blockade each partially restored them with similar efficacy; the combined treatment restored both to baseline levels (both P<0.001; Fig. 7E and F). BPTF knockdown also significantly increased the concentrations of both molecules, which were further elevated when BPTF knockdown was combined with methapyrilene treatment (Fig. S5D and E).

Flow cytometry further demonstrated that BPTF overexpression increased both the proportion of PD-$L1^+$ melanoma cells and the MFI of surface PD-L1, whereas methapyrilene significantly attenuated these changes (P<0.001; Fig. 7G). Therefore, the present findings indicated that tumor cell BPTF

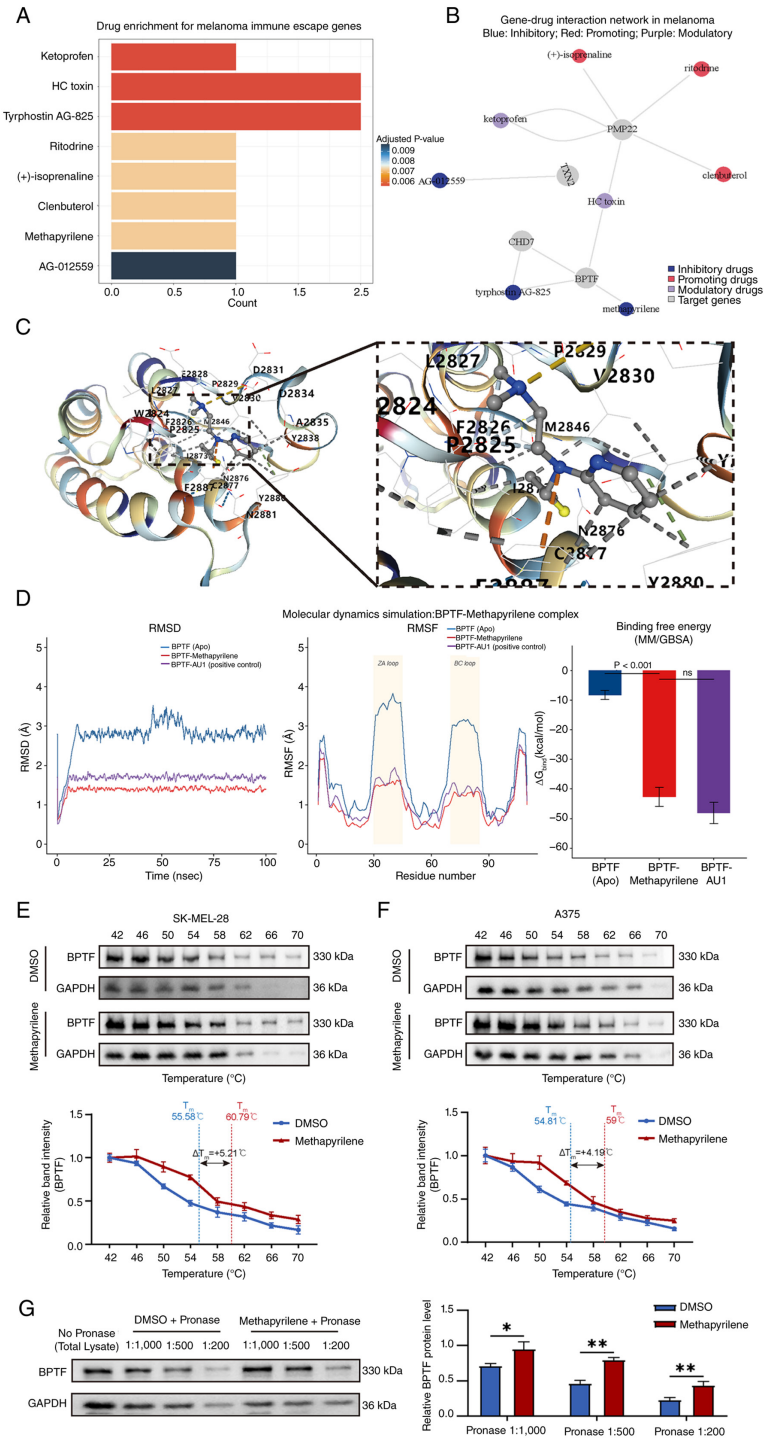


Figure 5. Drug-gene interaction, molecular docking and target-engagement analyses. (A) Drug enrichment. Bar plot demonstrates significantly enriched drugs that interact with immune escape genes. Bars are colored by significance level (adjusted P-value) and ordered according to statistical significance. (B) Drug-gene interaction network. Drug nodes are colored by classification: Blue for inhibitory drugs (potential therapeutic candidates), red for promoting drugs (potentially unfavorable candidates) and purple for modulatory drugs (require further validation). Edge represents drug-gene associations. (C) Molecular docking visualization. The 3D molecular docking result demonstrates the binding interaction between a selected drug compound and its protein target. The visualization displays the protein structure (ribbons/surface) and small molecule ligand (spheres/sticks) in their predicted binding conformation. The detailed view of molecular docking between methapyrilene and BPTF protein, demonstrates specific binding interactions, hydrogen bonds and contact residues. (D) Molecular dynamics simulations. From left to right: i) RMSD trajectories of apo BPTF, the BPTF-methapyrilene complex and the BPTF-AU1 complex; ii) RMSF curves for the three systems; and iii) binding free energies of the methapyrilene- and AU1-bound complexes estimated by the MM/GBSA method. Shaded regions in the RMSF plot indicate the ZA and BC loops, which connect helices αZ to αA and αB to αC, respectively, and flank the acetyl-lysine-binding pocket of the BPTF bromodomain. (E and F) Cellular thermal shift assays in (E) SK-MEL-28 and (F) A375 cells treated with DMSO or methapyrilene. BPTF abundance was normalized within each treatment group by setting the signal at 42˚C, which was set to 1. The ΔT_m values are displayed. (G) Drug affinity-responsive target stability analysis demonstrating the protection of BPTF from Pronase®-mediated degradation after methapyrilene treatment. The left panel indicates representative western blots of BPTF in SK-MEL-28 cell lysates pretreated with methapyrilene or DMSO and then digested with the indicated Pronase-to-total-protein concentrations. The right panel indicates quantification of BPTF band intensity normalized to the undigested control. *P<0.05 and **P<0.01 vs. DMSO at the same Pronase-to-total-protein ratio. HC toxin, *Cochliobolus carbonum* toxin; BPTF, bromodomain plant homeodomain finger transcription factor; RMSD, root-mean-square deviation; RMSF, root-mean-square fluctuation; MM/GBSA, molecular mechanics/generalized Born surface area; ΔT_m, change in apparent melting temperature; ns, not significant.

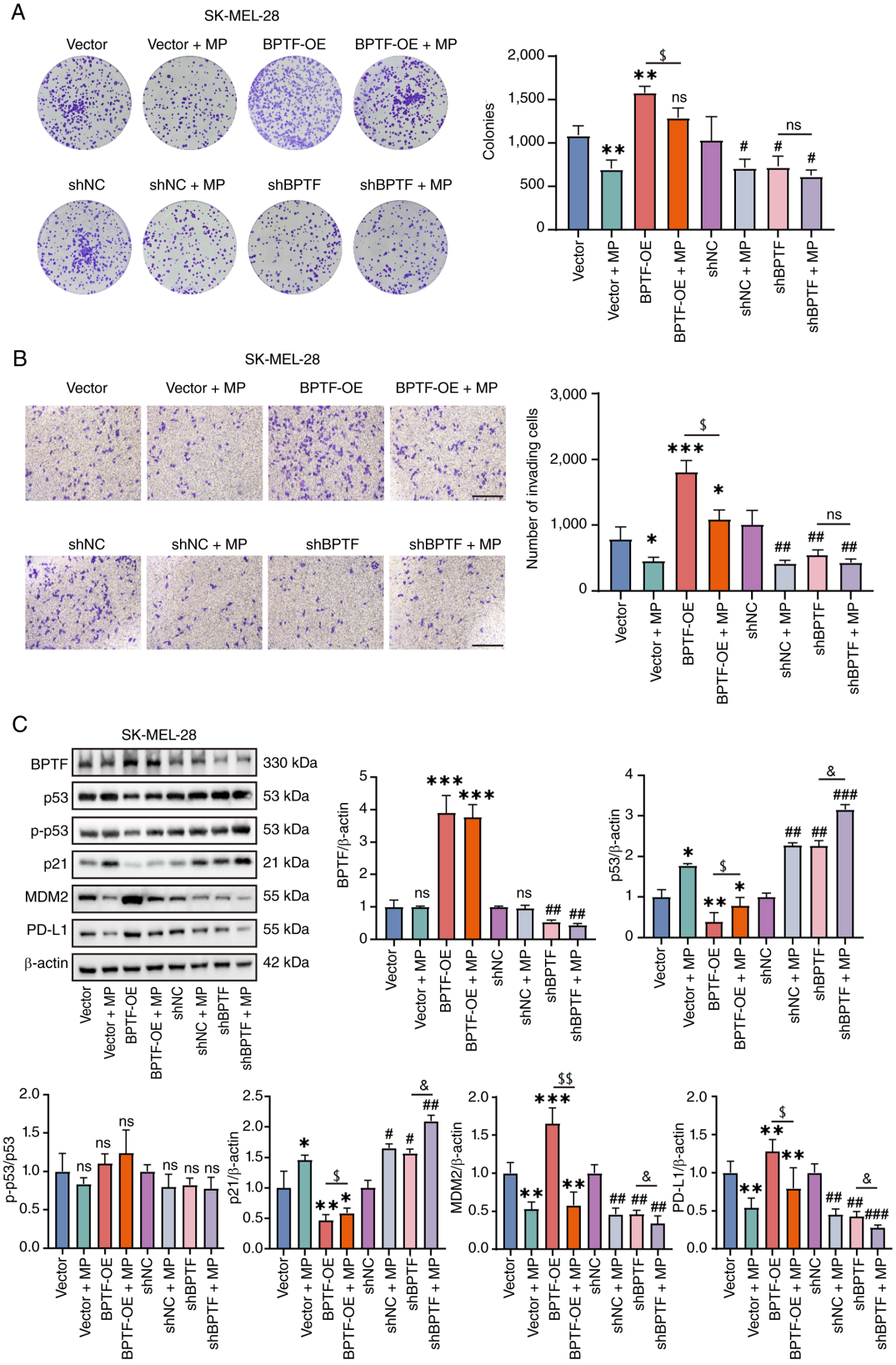


Figure 6. MP attenuates BPTF-mediated immune escape in SK-MEL-28 cells. (A) MP attenuates BPTF-mediated colony formation in SK-MEL-28 cells. Bar graphs show colony numbers (vs. vector, **P<0.01, BPTF-OE + MP vs. BPTF-OE, $^{\$}$P<0.05; vs. shNC, $^{\#}$P<0.05). shBPTF denotes shBPTF-1. (B) MP attenuates BPTF-mediated cell invasion in SK-MEL-28 cells. Bar graphs show numbers of invading cells (vs. vector, *P<0.05 and ***P<0.001, BPTF-OE + MP vs. BPTF-OE, $^{\$}$P<0.05; vs. shNC, $^{\#\#}$P<0.01). shBPTF denotes shBPTF-1. Magnification, x100; scale bars, 200 μm. (C) MP attenuates BPTF-mediated changes in immune-evasion-associated proteins in SK-MEL-28 cells. p-p53 (serine 15) was quantified relative to total p53, whereas the other proteins were normalized to β-actin. Bar graphs indicate relative protein-expression levels compared with the corresponding control (vs. vector, *P<0.05, **P<0.01 and ***P<0.001, BPTF-OE + MP vs. BPTF-OE, $^{\$}$P<0.05 and $^{\$\$}$P<0.01; vs. shNC, $^{\#}$P<0.05, $^{\#\#}$P<0.01 and $^{\#\#\#}$P<0.001, shBPTF + MP vs. shBPTF, $^{\&}$P<0.05). shBPTF denotes shBPTF-1. BPTF, bromodomain plant homeodomain finger transcription factor; MP, methapyrilene; p-p53, phosphorylated p53; BPTF-OE, BPTF-overexpressed; shNC, non-targeting short hairpin RNA control; shBPTF, BPTF knockdown; MDM2, mouse double minute 2, PD-L1, programmed death-ligand 1; ns, not significant.

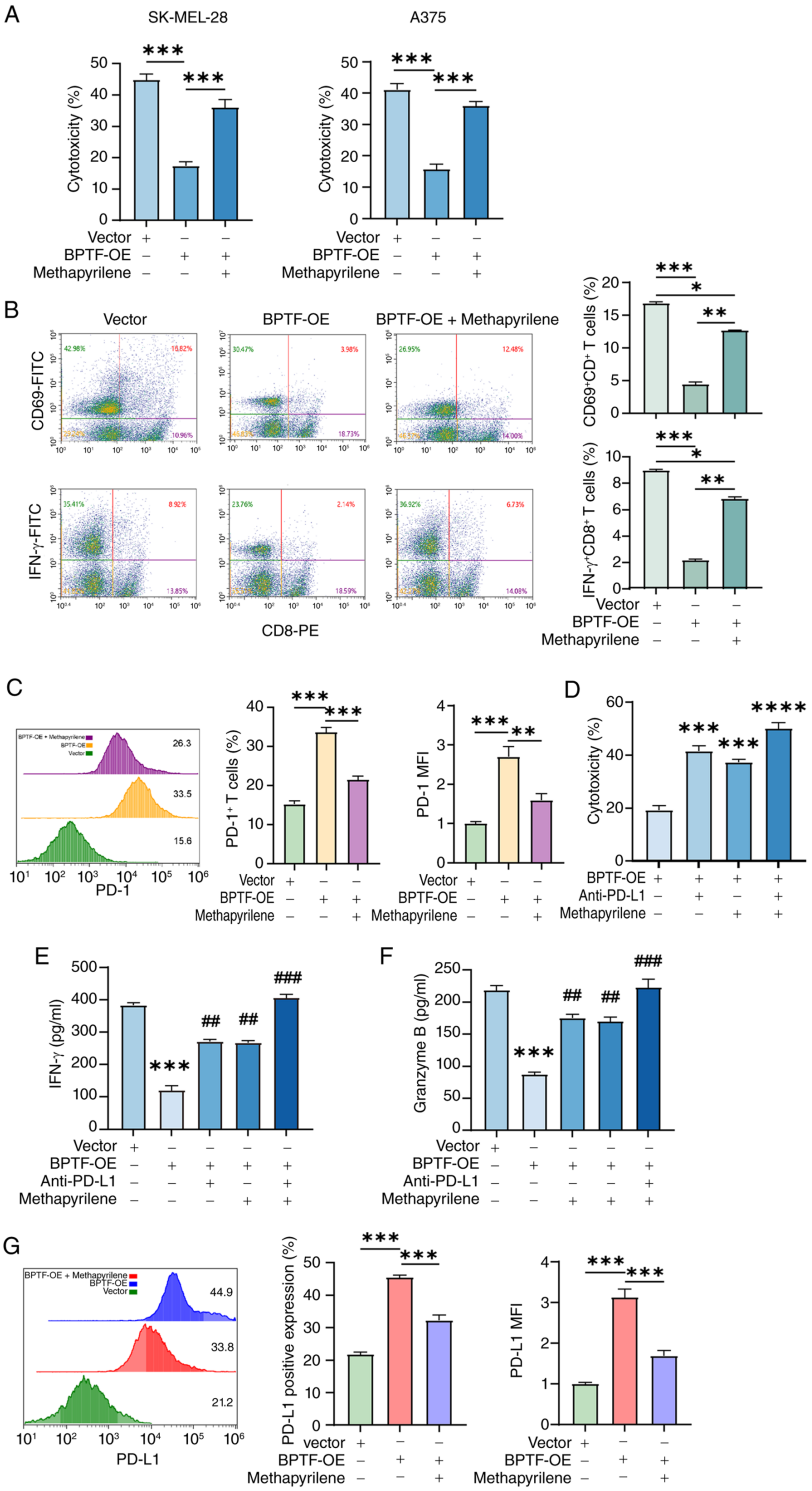


Figure 7. Methapyrilene reverses BPTF-mediated suppression of T-cell function. (A) Methapyrilene restores T-cell cytotoxicity suppressed by BPTF. The bar chart displays T-cell killing rates against SK-MEL-28 and A375 cells (***P<0.001). (B) Frequencies of CD69$^+$ CD8$^+$ cells and IFN-γ$^+$ CD8$^+$ T cells following co-culture with SK-MEL-28 cells. The upper panels present flow cytometry plots and quantitative bar charts of CD69$^+$ cells, whereas the lower panels indicate representative flow cytometry profiles and quantitative bar charts of IFN-γ$^+$ cells (*P<0.05, **P<0.01 and ***P<0.001). The double-positive percentages were calculated relative to the gated CD3$^+$ T-cell population. (C) Frequency of PD-1$^+$CD8$^+$ T cells and PD-1 MFI within the CD8$^+$ T-cell population following co-culture with SK-MEL-28 cells. Histograms and bar charts indicate the PD-1$^+$ T cells (%) and MFI, respectively (**P<0.01 and ***P<0.001). (D) Combined methapyrilene treatment and PD-L1 blockade further enhance T-cell killing rates against SK-MEL-28 cells (vs. BPTF-OE, ***P<0.001 and ****P<0.0001). (E) Combined methapyrilene treatment and PD-L1 blockade further restore IFN-γ secretion suppressed by BPTF in the SK-MEL-28 co-culture system (vs. vector, ***P<0.001; vs. BPTF-OE, ##P<0.01 and ###P<0.001). (F) Combined methapyrilene treatment and PD-L1 blockade restore granzyme B secretion suppressed by BPTF in the SK-MEL-28 co-culture system (vs. vector, ***P<0.001; vs. BPTF-OE, ##P<0.01 and ###P<0.001). (G) Methapyrilene attenuates BPTF-induced surface PD-L1 expression in SK-MEL-28 cells. Histograms and bar charts indicate PD-L1$^+$ cells (%) and the MFI, respectively (***P<0.001). PD-L1 was analyzed within viable, singlet CD45$^-$ tumor cells, with the positive threshold defined using the PD-L1-PE FMO control. For (B) and (C), lymphocyte, singlet and viability gates preceded CD3$^+$ T-cell selection; an additional CD8$^+$ gate was applied for (C). Quadrant boundaries in (B) and the PD-1-positive threshold in (C) were defined using the corresponding fluorescence-minus-one controls. BPTF, bromodomain plant homeodomain finger transcription factor; BPTF-OE, BPTF-overexpressed; PD-L1, programmed death-ligand 1; MFI, mean fluorescence intensity; PD-1, programmed cell death protein 1; IFN-γ, interferon-γ.

promotes melanoma immune evasion by suppressing $CD8^+$ T-cell effector function and T-cell-mediated tumor cell killing, at least partly through increased surface PD-L1. Methapyrilene partially reverses this phenotype.

Discussion

Melanoma immune escape arises from coordinated tumor-intrinsic and microenvironmental programs, thereby influencing clinical responses to immunotherapy (10,35). By integrating a number of immunotherapy cohorts with interpretable ML and experimental validation, the present study identified BPTF as a candidate tumor-intrinsic regulator of non-response to treatment. BPTF promoted malignant phenotypes and impaired $CD8^+$ T-cell function, accompanied by the attenuation of p53 signaling and activation of PD-L1. Methapyrilene engaged BPTF and attenuated these effects, while enhancing the effects of PD-L1 blockade *in vitro*. These findings extend the role of BPTF in melanoma progression to tumor cell immune evasion.

As the largest subunit of the nucleosome remodeling factor (NURF) complex, BPTF recognizes active chromatin and contributes to transcriptional regulation, development and immune-cell homeostasis (36,37). Previous studies on T-cell development and homeostasis have implicated that BPTF serves a key role in immune regulation (38,39). Elevated BPTF expression has also been associated with melanoma progression and poor survival (40). However, whether melanoma cell-intrinsic BPTF contributes to immune suppression remains to be elucidated. The present study addresses this gap by demonstrating that BPTF simultaneously promotes malignant behavior and restricts $CD8^+$ T-cell function through regulation of the p53/PD-L1 axis. The PD-1/PD-L1 pathway is a central mechanism through which melanoma cells suppress T-cell activation and cytotoxicity (41). Thus, the present findings associated the oncogenic activity of BPTF with tumor-intrinsic immune evasion.

Previous studies have reported that BPTF can cooperate with the transcription factor Yin-Yang 1 (YY1) and influence E3 ubiquitin ligase-related regulation in clear cell renal cell carcinoma (42,43). In melanoma, YY1 depletion disrupts the MDM2-p53 interaction, increases p53 activity, and induces p21 expression and cell-cycle arrest (43). In the present study, enrichment of ubiquitin-mediated proteolysis coincided with increased MDM2 expression, and attenuated p53 and p21 signaling. The unchanged relative Ser15 phosphorylation further suggests that BPTF primarily affects p53 abundance or stability rather than selectively regulating its Ser15 phosphorylation. This pattern suggests that BPTF facilitates MDM2-associated p53 turnover and weakens p53-dependent cell-cycle control, although direct regulation of p53 ubiquitination or degradation remains to be investigated. Beyond cell-cycle regulation, the MDM2/p53 axis influences antigen presentation, cytokine signaling and immune cell infiltration (44). Loss of p53 activity has also been associated with increased surface PD-L1 expression and immune escape in melanoma (45,46). The concurrent suppression of p53 signaling, elevation of PD-L1 and impairment of $CD8^+$ T-cell function observed here therefore collectively support a functional association between BPTF-driven tumor growth and immune suppression.

From a broader epigenetic perspective, chromatin remodeling influences tumor progression and treatment resistance (47), and NURF may enable BPTF to regulate the p53/PD-L1 axis at numerous levels. In the present study, ChIP-qPCR revealed increased BPTF enrichment at the TP53 and CD274 promoter regions following BPTF overexpression, whereas promoter-reporter assays demonstrated that BPTF overexpression suppressed *TP53* promoter activity but enhanced CD274 promoter activity. These findings support two routes of PD-L1 regulation: Direct promoter-associated activation of CD274 and an indirect route involving attenuation of p53 signaling. Reciprocal co-IP additionally demonstrated that BPTF and p53 were present within the same protein complex, suggesting that BPTF may regulate p53 not only transcriptionally but also at the protein level, thereby reinforcing p53 pathway suppression and PD-L1-mediated immune escape.

The mechanism of BPTF-mediated immune evasion should also be interpreted within the lineage-specific and systemic context of melanoma. Melanoma arises from pigment-producing melanocytes (48), and BPTF has been reported to be transcriptionally regulated by microphthalmia-associated transcription factor, a central regulator of melanocytic differentiation and melanogenesis (40,49). This lineage background is therefore biologically relevant. Mature melanin scavenges reactive species and chelates redox-active metals, whereas active melanogenesis generates reactive intermediates and may deplete thiol antioxidants, including glutathione (48,50). Therefore, in the present study, BPTF-high samples exhibited negative enrichment of glutathione metabolism pathway, suggesting altered oxidative homeostasis. These lineage-dependent differentiation and redox states actively reconfigure inflammatory signaling, elevate surface PD-L1 density and facilitate melanosomal drug sequestration (51-53). Beyond the local tumor microenvironment, advanced melanoma progressively disrupts systemic inflammatory, metabolic, neuroendocrine and immune homeostasis (54,55), creating a host-level immunosuppressive macroenvironment that exacerbates T-cell dysfunction and reduces checkpoint blockade efficacy. Such factors may modulate both BPTF-associated immune suppression and the activity of BPTF-directed compounds, providing a key biological context in interpreting the effects of methapyrilene.

Targeting BPTF may be valuable as this chromatin regulator may act upstream of both malignant growth programs and PD-L1-associated immune suppression. Disrupting BPTF may simultaneously reduce melanoma-cell fitness and alleviate tumor-intrinsic immune escape, potentially limiting compensatory signaling during ICB. However, methapyrilene should be regarded as a chemical probe and lead scaffold requiring further optimization, particularly due to its known hepatotoxicity and previous market withdrawal (56,57). Structural modeling, cellular target-engagement assays and genetic perturbation collectively support a BPTF-dependent component of methapyrilene activity, but do not establish absolute target selectivity. The established histamine H1 receptor activity of BPTF and reported effects on glutathione and iron metabolism further indicate potential polypharmacology (58). In the present study, the greater effect observed when methapyrilene was combined with PD-L1 blockade compared with either treatment alone supports the therapeutic concept of combining tumor-intrinsic

BPTF targeting with immune checkpoint inhibition. Medicinal chemistry optimization and evaluation in immunocompetent models are warranted to potentially develop safer and more selective BPTF-directed agents in the future.

Several limitations should be acknowledged in the present study. First, the ML model exhibited moderate discriminative performance. Therefore, it was used primarily to prioritize candidate genes rather than for clinical prediction. Heterogeneity in cohort size, treatment regimen, sampling time and response definition may have affected reproducibility. Second, the directionally constrained prioritizing genes upregulated in non-responders may have excluded downregulated protective or immune-effector genes. Third, the mechanistic evidence was derived mainly from melanoma cell lines and healthy-donor $CD8^+$ T-cell co-cultures. These findings were not validated using patient-derived tumor-infiltrating lymphocytes or immunocompetent *in vivo* models. The potential effects of driver mutations, pigmentation states and systemic tumor-host interactions were not systematically assessed. Lastly, molecular modeling, CETSA and DARTS supported the engagement of BPTF, whereas genetic perturbation indicated that methapyrilene activity was partially dependent on BPTF. However, these findings do not establish methapyrilene as a selective BPTF inhibitor. The known hepatotoxicity of methapyrilene further limits direct clinical translation, necessitating the development and evaluation of safer, more selective derivatives in the future.

In conclusion, by integrating multi-cohort transcriptomic analysis, an interpretable ML framework and experimental validation, the present study identified BPTF as a chromatin-associated regulator associating melanoma progression with *TP53* repression, *CD274*/PD-L1 activation and impaired $CD8^+$ T-cell function. Functional analyses indicated that BPTF suppressed p53 signaling, upregulated PD-L1 and impaired T-cell function. These coordinated effects promoted malignant tumor cell phenotypes and immune evasion, thereby contributing to an immunosuppressive tumor microenvironment. Methapyrilene attenuated BPTF-associated activity reversed its oncogenic effects and enhanced the antitumor effects of PD-L1 blockade. These results identify BPTF as a potential therapeutic target and provide proof-of-concept support for a drug-repurposing strategy to address immunotherapy resistance. Therefore, these findings provide a mechanistic basis in targeting BPTF in melanoma immune escape and support the potential development of safer, more selective BPTF-directed agents for use in combination with immunotherapy in the future.

Acknowledgements

Not applicable.

Funding

No funding was received.

Availability of data and materials

The data generated in the present study may be requested from the corresponding author.

Authors' contributions

XK and JH contributed to the conceptualization and methodology of the present study, performed the experiments, analyzed and interpreted the data and prepared the original draft. XY analyzed the molecular docking results, organized the experimental data and prepared the visualizations. XZ provided resources, performed experimental validation, analyzed and interpreted the validation data, and reviewed and edited the manuscript. BS contributed to the design of the study, participated in the interpretation of the study findings, supervised the study, oversaw data quality control, and critically reviewed and edited the manuscript. JY conceptualized the present study, provided supervision, and reviewed and edited the manuscript. BS and JY confirm the authenticity of all the raw data. All authors have read and approved the final manuscript, and are accountable for all aspects of the work.

Ethics approval and consent to participate

Not applicable.

Patient consent for publication

Not applicable.

Competing interests

The authors declare that they have no competing interests.

Use of artificial intelligence tools

During the preparation of this work, artificial intelligence tools were used to improve the readability and language of the manuscript, and subsequently, the authors revised and edited the content produced by the artificial intelligence tools as necessary, taking full responsibility for the ultimate content of the present manuscript.

References

1. Sun Y, Shen Y, Liu Q, Zhang H, Jia L, Chai Y, Jiang H, Wu M and Li Y: Global trends in melanoma burden: A comprehensive analysis from the global burden of disease study, 1990-2021. J Am Acad Dermatol 92: 100-107, 2025.
2. Zhou L, Zhong Y, Han L, Xie Y and Wan M: Global, regional, and national trends in the burden of melanoma and non-melanoma skin cancer: Insights from the global burden of disease study 1990-2021. Sci Rep 15: 5996, 2025.
3. Kunonga TP, Kenny RPW, Astin M, Bryant A, Kontogiannis V, Coughlan D, Richmond C, Eastaugh CH, Beyer FR, Pearson F, *et al*: Predictive accuracy of risk prediction models for recurrence, metastasis and survival for early-stage cutaneous melanoma: A systematic review. BMJ Open 13: e73306, 2023.
4. Di Raimondo C, Lozzi F, Di Domenico PP, Campione E and Bianchi L: The diagnosis and management of cutaneous metastases from melanoma. Int J Mol Sci 24: 14535, 2023.
5. Criado-Otero M, Navedo-de Las Heras M and Samaniego-González E: Topical and intralesional treatments for skin metastases and locoregionally advanced melanoma. Cancers (Basel) 17: 67, 2024.
6. Teixido C, Castillo P, Martinez-Vila C, Arance A and Alos L: Molecular markers and targets in melanoma. Cells 10: 2320, 2021.
7. Guo W, Wang H and Li C: Signal pathways of melanoma and targeted therapy. Signal Transduct Target Ther 6: 424, 2021.

8. Timar J and Ladanyi A: Molecular pathology of skin melanoma: Epidemiology, differential diagnostics, prognosis and therapy prediction. Int J Mol Sci 23: 5384, 2022.
9. Eddy K and Chen S: Overcoming immune evasion in melanoma. Int J Mol Sci 21: 8984, 2020.
10. Shirley CA, Chhabra G, Amiri D, Chang H and Ahmad N: Immune escape and metastasis mechanisms in melanoma: Breaking down the dichotomy. Front Immunol 15: 1336023, 2024.
11. Simiczyjew A, Dratkiewicz E, Mazurkiewicz J, Zietek M, Matkowski R and Nowak D: The influence of tumor microenvironment on immune escape of melanoma. Int J Mol Sci 21: 8359, 2020.
12. Jerby-Arnon L, Shah P, Cuoco MS, Rodman C, Su M, Melms JC, Leeson R, Kanodia A, Mei S, Lin J, *et al*: A cancer cell program promotes T cell exclusion and resistance to checkpoint blockade. Cell 175: 984-997, 2018.
13. Pan D, Kobayashi A, Jiang P, Ferrari de Andrade L, Tay RE, Luoma AM, Tsoucas D, Qiu X, Lim K, Rao P, *et al*: A major chromatin regulator determines resistance of tumor cells to T cell-mediated killing. Science 359: 770-775, 2018.
14. Zhang S, Cai WL, Liu X, Thakral D, Luo J, Chan LH, McGeary MK, Song E, Blenman KRM, Micevic G, *et al*: KDM5B promotes immune evasion by recruiting SETDB1 to silence retroelements. Nature 598: 682-687, 2021.
15. Li C, Wang Z, Yao L, Lin X, Jian Y, Li Y, Zhang J, Shao J, Tran PD, Hagman JR, *et al*: Mi-2β promotes immune evasion in melanoma by activating EZH2 methylation. Nat Commun 15: 2163, 2024.
16. Swanson K, Wu E, Zhang A, Alizadeh AA and Zou J: From patterns to patients: Advances in clinical machine learning for cancer diagnosis, prognosis, and treatment. Cell 186: 1772-1791, 2023.
17. Ma EZ, Hoegler KM and Zhou AE: Bioinformatic and machine learning applications in melanoma risk assessment and prognosis: A literature review. Genes (Basel) 12: 1751, 2021.
18. Hounye AH, Xiong L and Hou M: Integrated explainable machine learning and multi-omics analysis for survival prediction in cancer with immunotherapy response. Apoptosis 30: 364-388, 2025.
19. Riaz N, Havel JJ, Makarov V, Desrichard A, Urba WJ, Sims JS, Hodi FS, Martín-Algarra S, Mandal R, Sharfman WH, *et al*: Tumor and microenvironment evolution during immunotherapy with nivolumab. Cell 171: 934-949.e16, 2017.
20. Van Allen EM, Miao D, Schilling B, Shukla SA, Blank C, Zimmer L, Sucker A, Hillen U, Foppen MHG, Goldinger SM, *et al*: Genomic correlates of response to CTLA-4 blockade in metastatic melanoma. Science 350: 207-211, 2015.
21. Gide TN, Quek C, Menzies AM, Tasker AT, Shang P, Holst J, Madore J, Lim SY, Velickovic R, Wongchenko M, *et al*: Distinct immune cell populations define response to Anti-PD-1 monotherapy and Anti-PD-1/Anti-CTLA-4 combined therapy. Cancer Cell 35: 238-255.e6, 2019.
22. Jaiswal AR, Liu AJ, Pudakalakatti S, Dutta P, Jayaprakash P, Bartkowiak T, Ager CR, Wang Z, Reuben A, Cooper ZA, *et al*: Melanoma evolves complete immunotherapy resistance through the acquisition of a hypermetabolic phenotype. Cancer Immunol Res 8: 1365-1380, 2020.
23. Eisenhauer EA, Therasse P, Bogaerts J, Schwartz LH, Sargent D, Ford R, Dancey J, Arbuck S, Gwyther S, Mooney M, *et al*: New response evaluation criteria in solid tumours: Revised RECIST guideline (version 1.1). Eur J Cancer 45: 228-247, 2009.
24. Hugo W, Zaretsky JM, Sun L, Song C, Moreno BH, Hu-Lieskovan S, Berent-Maoz B, Pang J, Chmielowski B, Cherry G, *et al*: Genomic and transcriptomic features of response to Anti-PD-1 therapy in metastatic melanoma. Cell 165: 35-44, 2016.
25. Hirose S, Mashima T, Yuan X, Yamashita M, Kitano S, Torii S, Migita T and Seimiya H: Interleukin-4 induced 1-mediated resistance to an immune checkpoint inhibitor through suppression of CD8+ T cell infiltration in melanoma. Cancer Sci 115: 791-803, 2024.
26. Zhu T, Wei T, Yang M, Xu J, Jiang H, He W, Zheng J and Dai H: ETV4-Mediated PD-L1 upregulation promotes immune evasion and predicts poor immunotherapy response in melanoma. Oncol Res 34: 25, 2025.
27. Guyon I, Weston J, Barnhill S and Vapnik V: Gene selection for cancer classification using support vector machines. Mach Learn 46: 389-422, 2002.
28. Martin FJ, Amode MR, Aneja A, Austine-Orimoloye O, Azov AG, Barnes I, Becker A, Bennett R, Berry A, Bhai J, *et al*: Ensembl 2023. Nucleic Acids Res 51: D933-D941, 2023.
29. Benjamini Y and Hochberg Y: Controlling the false discovery rate: A practical and powerful approach to multiple testing. J R Stat Soc Series B Methodol 57: 289-300, 1995.
30. Case DA, Cheatham TER, Darden T, Gohlke H, Luo R, Merz KMJ, Onufriev A, Simmerling C, Wang B and Woods RJ: The amber biomolecular simulation programs. J Comput Chem 26: 1668-1688, 2005.
31. Case DA, Aktulga HM, Belfon K, Cerutti DS, Cisneros GA, Cruzeiro VWD, Forouzesh N, Giese TJ, Götz AW, Gohlke H, *et al*: AmberTools. J Chem Inf Model 63: 6183-6191, 2023.
32. Miller BRR, McGee TDJ, Swails JM, Homeyer N, Gohlke H and Roitberg AE: MMPBSA.py: An efficient program for End-state free energy calculations. J Chem Theory Comput 8: 3314-3321, 2012.
33. Wu HH, Leng S, Eisenstat DD, Sergi C and Leng R: Targeting p53 for immune modulation: Exploring its functions in tumor immunity and inflammation. Cancer Lett 617: 217614, 2025.
34. Langenbach M, Giesler S, Richtsfeld S, Costa-Pereira S, Rindlisbacher L, Wertheimer T, Braun LM, Andrieux G, Duquesne S, Pfeifer D, *et al*: MDM2 inhibition enhances immune checkpoint inhibitor efficacy by increasing IL15 and MHC Class II production. Mol Cancer Res 21: 849-864, 2023.
35. Roerden M and Spranger S: Cancer immune evasion, immunoediting and intratumour heterogeneity. Nat Rev Immunol 25: 353-369, 2025.
36. Li F, Yu J, Pan T, Feng H, Li J, Yu B, Fan Z, Sang Q, Chen M, Zang M, *et al*: BPTF drives gastric cancer resistance to EGFR inhibitor by epigenetically regulating the C-MYC/PLCG1/Perk axis. Adv Sci (Weinh) 10: e2303091, 2023.
37. Liang X, Cao Y, Duan Z, Wang M, Zhang N, Ding Y, Luo C, Lu N and Chen S: Discovery of new small molecule inhibitors of the BPTF bromodomain. Bioorg Chem 134: 106453, 2023.
38. Wu B, Wang Y, Wang C, Wang GG, Wu J and Wan YY: BPTF is essential for T cell homeostasis and function. J Immunol 197: 4325-4333, 2016.
39. Mayes K, Alkhatib SG, Peterson K, Alhazmi A, Song C, Chan V, Blevins T, Roberts M, Dumur CI, Wang X, *et al*: BPTF depletion enhances T-cell-Mediated antitumor immunity. Cancer Res 76: 6183-6192, 2016.
40. Zahid H, Olson NM and Pomerantz WCK: Opportunity knocks for uncovering the new function of an understudied nucleosome remodeling complex member, the bromodomain PHD finger transcription factor, BPTF. Curr Opin Chem Biol 63: 57-67, 2021.
41. Lau P, Zhang G, Zhao S, Liang L, Zhang H, Zhou G, Hung M, Chen X and Liu H: Sphingosine kinase 1 promotes tumor immune evasion by regulating the MTA3-PD-L1 axis. Cell Mol Immunol 19: 1153-1167, 2022.
42. Yang Y, Wang C, Wei N, Hong T, Sun Z, Xiao J, Yao J, Li Z and Liu T: Identification of prognostic chromatin-remodeling genes in clear cell renal cell carcinoma. Aging (Albany NY) 12: 25614-25642, 2020.
43. Zhou S, Li P, Qin L, Huang S and Dang N: Transcription factor YY1 contributes to human melanoma cell growth through modulating the p53 signalling pathway. Exp Dermatol 31: 1563-1578, 2022.
44. Brummer T and Zeiser R: The role of the MDM2/p53 axis in antitumor immune responses. Blood 143: 2701-2709, 2024.
45. Zeng Q, Zeng S, Dai X, Ding Y, Huang C, Ruan R, Xiong J, Tang X and Deng J: MDM2 inhibitors in cancer immunotherapy: Current status and perspective. Genes Dis 11: 101279, 2024.
46. Martinkova L, Zatloukalova P, Kucerikova M, Friedlova N, Tylichova Z, Zavadil-Kokas F, Hupp TR, Coates PJ and Vojtesek B: Inverse correlation between TP53 gene status and PD-L1 protein levels in a melanoma cell model depends on an IRF1/SOX10 regulatory axis. Cell Mol Biol Lett 29: 117, 2024.
47. Zhang F and Li D: Targeting chromatin-remodeling factors in cancer cells: Promising molecules in cancer therapy. Int J Mol Sci 23: 12815, 2022.
48. Slominski A, Tobin DJ, Shibahara S and Wortsman J: Melanin pigmentation in mammalian skin and its hormonal regulation. Physiol Rev 84: 1155-1228, 2004.
49. Dar AA, Majid S, Bezrookove V, Phan B, Ursu S, Nosrati M, De Semir D, Sagebiel RW, Miller JRR, Debs R, *et al*: BPTF transduces MITF-driven prosurvival signals in melanoma cells. Proc Natl Acad Sci USA 113: 6254-6258, 2016.
50. Slominski RM, Sarna T, Płonka PM, Raman C, Brożyna AA and Slominski AT: Melanoma, melanin, and melanogenesis: The yin and yang relationship. Front Oncol 12: 842496, 2022.

51. Sævarsson T, de Lomana ALG, Sánchez Ó, van Esch V, Ragnarsson GB, Brynjólfsson SF, Steingrímsson E and Einarsdóttir BÓ: Differentiation status determines the effects of IFNγ on the expression of PD-L1 and immunomodulatory genes in melanoma. Cell Commun Signal 22: 618, 2024.
52. Ghaffarian-Bahraman A, Arabnezhad M, Keshavarzi M, Davani-Davari D, Jamshidzadeh A and Mohammadi-Bardbori A: Influence of cellular redox environment on aryl hydrocarbon receptor ligands induced melanogenesis. Toxicol In Vitro 79: 105282, 2022.
53. Slominski RM, Kim T, Janjetovic Z, Brożyna AA, Podgorska E, Dixon KM, Mason RS, Tuckey RC, Sharma R, Crossman DK, *et al*: Malignant melanoma: An overview, new perspectives, and vitamin D signaling. Cancers (Basel) 16: 2262, 2024.
54. Slominski RM, Raman C, Chen JY and Slominski AT: How cancer hijacks the body's homeostasis through the neuroendocrine system. Trends Neurosci 46: 263-275, 2023.
55. Rossi N, Lee KA, Bermudez MV, Visconti A, Thomas AM, Bolte LA, Björk JR, de Ruijter LK, Newton-Bishop J, Harland M, *et al*: Circulating inflammatory proteins associate with response to immune checkpoint inhibition therapy in patients with advanced melanoma. EBioMedicine 83: 104235, 2022.
56. Braeuning A, Oberemm A, Heise T, Gundert-Remy U, Hengstler JG and Lampen A: In vitro proteomic analysis of methapyrilene toxicity in rat hepatocytes reveals effects on intermediary metabolism. Arch Toxicol 93: 369-383, 2019.
57. Winek CL, Fochtman FW, Trogus WJJ, Fusia EP and Shanor SP: Methapyrilene toxicity. Clin Toxicol (Phila) 11: 287-294, 1977.
58. Yafune A, Taniai E, Morita R, Akane H, Kimura M, Mitsumori K and Shibutani M: Immunohistochemical cellular distribution of proteins related to M phase regulation in early proliferative lesions induced by tumor promotion in rat two-stage carcinogenesis models. Exp Toxicol Pathol 66: 1-11, 2014.

Copyright © 2026 Kang et al. This work is licensed under a Creative Commons Attribution-NonCommercial-NoDerivatives 4.0 International (CC BY-NC-ND 4.0) License.